Modeling, Oscillation Analysis and Distributed Stabilization Control of Autonomous PV-based Microgrids

Zhuoli Zhao, *Member*, *IEEE*, Jindian Xie, Shaoqing Gong, Xi Luo, Yuewu Wang, Chun Sing Lai, *Senior Member*, *IEEE*, Ping Yang, Loi Lei Lai, *Life Fellow*, *IEEE*, and Josep M. Guerrero, *Fellow*, *IEEE*

***Abstract*—Driven by rising energy demand and the goal of carbon neutrality, renewable energy generations (REGs), especially photovoltaic (PV) generations, are widely used in the urban power energy systems. While the intelligent control of microgrids (MG) brings economic and efficient operation, its potential stability problem cannot be ignored. To date, most of the research on modeling, analyzing and enhancing the stability of MG usually assume the DC-link as an ideal voltage source. However, this practice of ignoring the dynamics of DC-link may omit the latent oscillation phenomena of autonomous PV-based MG. First, this paper establishes a complete dynamic model of autonomous PV-based MG including PV panels and DC-link. Different from previous conclusions of idealizing DC-link dynamics, participation factor analysis finds the potential impact of DC-link dynamics on system dynamic performance, and different influence factors including critical control parameters and nonlinear V-I output characteristic of PV array are considered to further reveal oscillation mechanisms. Second, based on the average consensus algorithm, a distributed stabilization controller with strong robustness is proposed to enhance stability of the PV-based MG, which does not affect the steady-state performance of the system. Finally, the correctness of all theoretical analysis and the effectiveness of the proposed controller are verified by time domain simulation and hardware-in-loop tests.**

***Index Terms*—Average consensus algorithm, distributed stabilization, microgrid, oscillation, photovoltaic (PV) generation, stability analysis.**

I. Introduction

In order to meet the growing demand for energy and carbon neutrality targets, renewable energy generations (REGs) have been rapidly deployed all over the world because of their clean and pollution-free characteristics [1]. In recent years, continuous technological innovation has provided photovoltaic (PV) panels with higher conversion efficiency as well as lower price, making solar energy widely applicable in urban power energy systems, such as PV rooftops [2]–[4], PV power stations [5]–[7], PV charging stations [8]–[10], etc.

Microgrids (MGs) are a concept designed for coping with high penetration of REG, providing an approach for integrating distributed generations (DGs) and energy storage systems (ESSs). According to actual needs, MGs can operate flexibly in grid-connected mode or autonomous mode by introducing the hierarchical control framework including primary control, secondary control and tertiary control into the control loop [11]. These intelligent control methods can effectively improve reliability and economy of the microgrid (MG). Although the above schemes have achieved satisfactory performance, the autonomous MG still faces potential stability problems [12]–[15], which pose a threat to effective operation and restoration of MG and urban distribution power systems. Reference [12] studied the influence of droop control on system stability, pointing out that weak damping of dominant modes related to power sharing dynamics may lead to oscillation and even system collapse with increase of load. Meanwhile, as the inverter interface is adopted between DGs, wide use of inverters will bring harmonic interaction with other devices, which may trigger oscillation problems [13]. Negative incremental input impedances caused by constant power loads will also reduce system damping and make the system more prone to oscillation [14]. In addition, application of distributed secondary control may introduce new poor damping modes and causes oscillatory responses [15].

Much work so far has focused on overcoming the aforementioned challenges [15]–[19]. In [15], the distributed optimal controller was introduced to obtain desirable damping and dynamic performance. Reference [16] presented an emerging virtual impedance damping method to cope with power angle oscillation. A hybrid damping controller including state feedback control and PI control was used in [17]. Reference [18] proposed an active damping method based on a

Manuscript received October 9, 2021; revised January 18, 2022; accepted April 23, 2022. Date of online publication August 18, 2022; date of current version September 19, 2022. This work was supported by the National Natural Science Foundation of China (51907031); Guangdong Basic and Applied Basic Research Foundation (Guangdong-Guangxi Joint Foundation) (2021A1515410009).

Z. Zhao, J. Xie, X. Luo, S. Gong, and L. L. Lai are with the Department of Electrical Engineering, School of Automation, Guangdong University of Technology, Guangzhou 510006, China.

Y. Wang is with the School of Automation, Guangxi University of Science and Technology, Liuzhou 545006, China.

C. S. Lai (corresponding author, email: chunsing.lai@brunel.ac.uk) is with the Department of Electronic and Electrical Engineering, Brunel University London, London UB8 3PH, UK; and also with the Department of Electrical Engineering, School of Automation, Guangdong University of Technology, Guangzhou 510006, China.

P. Yang is with the Key Laboratory of Clean Energy Technology of Guangdong Province, South China University of Technology, Guangzhou 510640, China.

J. M. Guerrero is with the Department of Energy Technology, Aalborg University, 9220 Aalborg, Denmark.

DOI: 10.17775/CSEEJPES.2021.07570

robust disturbance observer to dampen oscillations caused by interactions between interconnecting passive filters, as well as the presence of disturbing load. A supplementary controller comprised of three lead-lag blocks was proposed in [19] for handling oscillation caused by high gains of the droop control loop.

The aforementioned studies can stabilize MGs effectively, while most of them simplified the DC-link into an ideal voltage source in the process of modeling and analysis. It should be noted this simplified model may not be able to accurately capture the actual dynamic response of MGs with PV generation. Typically, control strategies of PV inverters can be classified into grid-following control [20]–[23] and grid-forming control [24]–[27]. As a result of the intermittent nature of solar irradiation and the transient response of the maximum power point tracking (MPPT) strategy, the voltage of the DC-link will change continuously [28], [29]. Up to now, a lot of studies have been carried out to address the DC-link voltage fluctuation [30]–[32], and both [33] and [34] have pointed out that simplification will lose critical dynamic behavior of DC-link for grid-following PV inverters. On the other hand, in order to achieve seamless switching between autonomous MG mode and grid-connected MG mode, and reduce the risk of outage caused by master power source failure in autonomous MG mode, DGs are recommended to operate in grid-forming control since it enables DGs to regulate grid voltage and frequency [35]. For most conventional grid-forming PV inverters, energy storage is needed for connection to the DC-link to prevent the DC-link voltage from collapsing [24]–[26]. Besides, a novel DC-link voltage controller was proposed in [27] to make it possible for grid-forming PV inverters to stabilize DC-link voltage without assistance of energy storage. However, the common practice for assuming the DC-link voltage to be constant due to the energy buffer cannot simply be mapped straight onto the latter for modeling. Otherwise, the analysis may lead to inaccurate results [36]. In [36], comparison of PV-based MG dominant modes with and without considering DC-link dynamics shows that low-frequency eigenvalues are introduced when considering DC-link dynamics. However, the mechanism of the potential oscillation behavior of the PV-based MG system under the solar irradiance fluctuation has not been studied. Moreover, a tie-line flow and stabilization strategy based on a centralized controller was proposed in [36] for restraining oscillation caused by DC-links. Since the central controller may suffer from computation burdens and risk of single-point failure, reliability of the centralized controller is lower than that of the distributed controller using the information of neighboring nodes through a sparse communication network [37].

So far, limited research has been conducted in applying distributed structure for stabilization [38]–[40]. In [38], the stability of inverter-based MGs is improved by a distributed successive linear programming algorithm through tuning the cut-off frequency of the low-pass filters. Reference [39] proposed a distributed damping control unit (DCU) for wind generators and load aggregators in power systems and the parameters of DCU are tuned to improve the damping ratio of the critical low-frequency inter-area oscillations (LFOs). A secondary frequency controller for VSG-based MGs with event-triggered communication mechanism is proposed in [40] and oscillation can be damped during frequency restoration. Once again, the above studies do not involve PV generations and DC-link dynamics. Therefore, the distributed stabilization controller used for autonomous PV-based MGs deserves further investigation.

Considering that urban power energy systems will integrate a large number of PV generations in the near future, the purpose of this paper is to reveal possible oscillation of grid-forming PV unit in autonomous MG, and to propose a distributed stabilization controller to enhance stability of MG. Specifically, this paper establishes a detailed model of grid-forming PV-based MG. Based on the small-signal dynamic model, stability analysis is employed for discovering critical dynamics, finding out essential influence factors and revealing oscillation mechanisms of autonomous PV-based MG. Furthermore, to improve the system characteristics performance, a distributed stabilization controller based on the average consensus algorithm is proposed. Finally, time-domain simulation is also used to present undesirable oscillation. The correctness of the above analysis and effectiveness of the proposed controller are verified in hardware-in-the-loop (HIL) tests.

The main contributions of this paper are summarized as follows:

1) A detailed model of autonomous PV-based MG considering solar irradiance changes, DC-link dynamics, primary control, networks and loads, which can more accurately reflect the dynamic characteristics of the PV-based MG.

2) Discovery of undesirable oscillation under specific solar irradiance fluctuation conditions. Oscillation is caused by DC-link dynamics and will be activated between different PV generators by inappropriate control parameters and the disturbance of uneven sunlight change with different initial DC-link voltage, which cannot be observed in the model by assuming DC-links as the ideal voltage sources.

3) An intelligent distributed stabilization controller with strong robustness and good performance to restrain oscillation. The proposed controller only works during the transient period and does not affect steady-state performance of the system, which is still effective in case of communication link failure.

The rest of this paper is organized as follows: A detailed model of autonomous PV-based microgrid is developed in Section II. Different influence factors on DC-link dynamics are analyzed and the mechanism of the oscillation is revealed in Section III. Section IV presents the proposed distributed stabilization controller. In Section V, several comparisons are made to test the analysis and proposed controller in time-domain simulations. The HIL tests are provided in Section VI. Finally, Section VII concludes the paper.

II. Dynamic Model of Autonomous PV-Based MG

A typical residential PV-based MG topology of the future urban power energy system is presented in Fig. 1. Three DGs are connected to the point of common coupling (PCC) to supply power for users' loads. PCC is connected with the

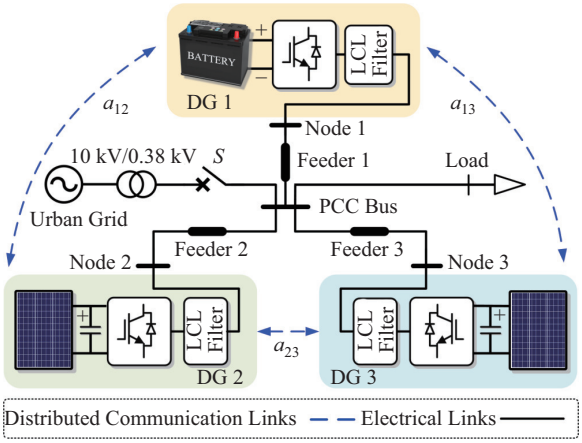

Fig. 1. A typical residential PV-based microgrid.

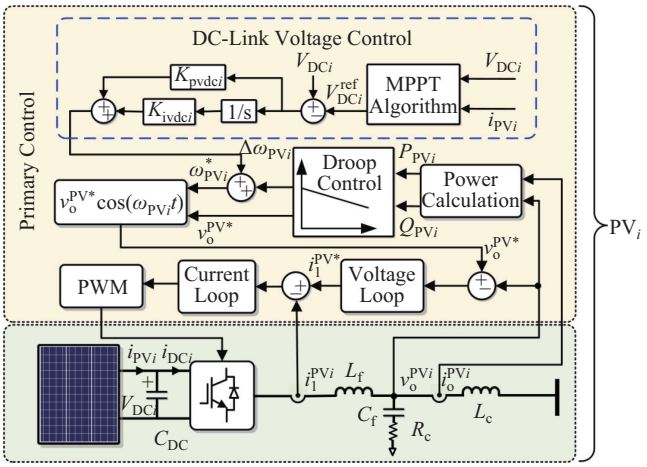

Fig. 2. Control structure of PV_i.

urban distribution power systems through a transformer and bypass switch. The on-off condition of the bypass switch determines whether the MG works in grid-connected mode or autonomous mode. This paper will study the autonomous mode. DG1 is the battery energy storage system (BESS), which can provide extra energy reserves under low irradiance. DG2 and DG3 represent single-stage PV systems, which generally work in MPPT mode to ensure highest utilization of solar energy. It is worth noting that both PV systems and BESS operate in grid-forming control strategy depicted in Fig. 2 and each part of the MG system will be modeled in detail below.

A. Model of Individual DG

The non-linear V-I characteristic of the PV array can be described as the following mathematical equation:

$$i_{\mathrm{PV}i} = N_{\mathrm{p}i} I_{\mathrm{ph}i} - N_{\mathrm{p}i} I_{\mathrm{rs}i} \left[\exp\left(qV_{\mathrm{DC}i}/kT_{\mathrm{T}i}A_{\mathrm{IF}}N_{\mathrm{s}i}N_{\mathrm{c}i}\right) - 1\right] \tag{1}$$

where the variable $x_{\mathrm{PV}i}$ or $x^{\mathrm{PV}i}$ in the following text refer to the variable of the ith PV system.$i_{\mathrm{PV}i}$ is the output current of PV panel; $N_{\mathrm{p}i}$, $N_{\mathrm{s}i}$ and $N_{\mathrm{c}i}$ are the number of parallel strings, the amount of series connection modules in each string, and the amount of series-cells in each module; $I_{\mathrm{rs}i}$ and $I_{\mathrm{ph}i}$ represent the diode reverse saturation current and the short-circuit current per string; q and k are the value of the unit electric charge and Boltzman's constant, respectively; $T_{\mathrm{T}i}$ and A_{IF} are the temperature of the p–n junction and the ideality factor.

Different from the ideal voltage source, the DC side voltage of PV unit will change during transient and the power balance equation of DC-link dynamic is:

$$\begin{cases} \dot{V}_{\mathrm{DC}i} = (i_{\mathrm{PV}i} - i_{\mathrm{DC}i})/C_{\mathrm{DC}i} \\ i_{\mathrm{DC}i} = (v_{\mathrm{id}}^{\mathrm{PV}i} i_{\mathrm{ld}}^{\mathrm{PV}i} + v_{\mathrm{iq}}^{\mathrm{PV}i} i_{\mathrm{lq}}^{\mathrm{PV}i})/V_{\mathrm{DC}i} \end{cases} \tag{2}$$

where $C_{\mathrm{DC}i}$ is the capacitor of the DC-link, $i_{\mathrm{DC}i}$ is the inverter-side input currents, $v_{\mathrm{id}}^{\mathrm{PV}i}$ and $v_{\mathrm{iq}}^{\mathrm{PV}i}$ are the inverter-side output voltages, $i_{\mathrm{ld}}^{\mathrm{PV}i}$ and $i_{\mathrm{lq}}^{\mathrm{PV}i}$ are the filter inductor currents.

The instantaneous active power $p_{\mathrm{PV}i}$ and reactive power $q_{\mathrm{PV}i}$ of the PV unit are given by

$$\begin{cases} p_{\mathrm{PV}i} = v_{\mathrm{od}}^{\mathrm{PV}i} i_{\mathrm{od}}^{\mathrm{PV}i} + v_{\mathrm{oq}}^{\mathrm{PV}i} i_{\mathrm{oq}}^{\mathrm{PV}i} \\ q_{\mathrm{PV}i} = v_{\mathrm{oq}}^{\mathrm{PV}i} i_{\mathrm{od}}^{\mathrm{PV}i} - v_{\mathrm{od}}^{\mathrm{PV}i} i_{\mathrm{oq}}^{\mathrm{PV}i} \end{cases} \tag{3}$$

where $v_{\mathrm{od}}^{\mathrm{PV}i}$ and $v_{\mathrm{oq}}^{\mathrm{PV}i}$ are the output converter voltage in local frame, while $i_{\mathrm{od}}^{\mathrm{PV}i}$ and $i_{\mathrm{oq}}^{\mathrm{PV}i}$ are the output currents of PV system.

To ensure high-quality power injection, the filtered active power $P_{\mathrm{PV}i}$ and reactive power $Q_{\mathrm{PV}i}$ can be expressed as

$$\begin{cases} \dot{P}_{\mathrm{PV}i} = \omega_{\mathrm{c}} v_{\mathrm{od}}^{\mathrm{PV}i} i_{\mathrm{od}}^{\mathrm{PV}i} + \omega_{\mathrm{c}} v_{\mathrm{oq}}^{\mathrm{PV}i} i_{\mathrm{oq}}^{\mathrm{PV}i} - \omega_{\mathrm{c}} P_{\mathrm{PV}i} \\ \dot{Q}_{\mathrm{PV}i} = \omega_{\mathrm{c}} v_{\mathrm{oq}}^{\mathrm{PV}i} i_{\mathrm{od}}^{\mathrm{PV}i} - \omega_{\mathrm{c}} v_{\mathrm{od}}^{\mathrm{PV}i} i_{\mathrm{oq}}^{\mathrm{PV}i} - \omega_{\mathrm{c}} Q_{\mathrm{PV}i} \end{cases} \tag{4}$$

where ω_{c} is the cut-off frequency of the low-pass filter.

DC-link voltage controller is essential for single-stage PV systems to prevent DC-link voltage from collapsing due to overload during transition and also provides the function for PV systems to operate in MPPT mode, which is given by [27].

$$\Delta\omega_{\mathrm{PV}i} = K_{\mathrm{pvdc}i}\left(V_{\mathrm{DC}i} - V_{\mathrm{DC}i}^{\mathrm{ref}}\right) + K_{\mathrm{ivdc}i}\int (V_{\mathrm{DC}i} - V_{\mathrm{DC}i}^{\mathrm{ref}})\mathrm{d}t \tag{5}$$

where $\Delta\omega_{\mathrm{PV}i}$ is the output of this controller, while $K_{\mathrm{pvdc}i}$ and $K_{\mathrm{ivdc}i}$ are gain values; $V_{\mathrm{DC}i}$ is the DC-link voltage and $V_{\mathrm{DC}i}^{\mathrm{ref}}$ is the reference DC-link voltage offered by MPPT controller.

The droop control loop that makes PV systems obtain good power sharing with other DGs can be seen as follows:

$$\begin{cases} \omega_{\mathrm{PV}i}^{*} = \omega_n^{\mathrm{PV}i} - m_{\mathrm{P}}^{\mathrm{PV}i}(P_{\mathrm{PV}i} - P_{\mathrm{PV}i}^{*}) + \Delta\omega_{\mathrm{PV}i} \\ v_{\mathrm{o}}^{\mathrm{PV}i*} = V_n^{\mathrm{PV}i} - n_{\mathrm{Q}}^{\mathrm{PV}i}(Q_{\mathrm{PV}i} - Q_{\mathrm{PV}i}^{*}) \end{cases} \tag{6}$$

where $\omega_{\mathrm{PV}i}^{*}$ is the output angular frequency, and $v_{\mathrm{o}}^{\mathrm{PV}i*}$ is reference signal for the voltage control loop; $\omega_n^{\mathrm{PV}i}$ and $V_n^{\mathrm{PV}i}$ are the nominal frequency and voltage, $m_{\mathrm{P}}^{\mathrm{PV}i}$ and $n_{\mathrm{Q}}^{\mathrm{PV}i}$ are the active and reactive power droop coefficients; $P_{\mathrm{PV}i}^{*}$ and $Q_{\mathrm{PV}i}^{*}$ are the active and reactive power reference, respectively.

Remark 1. The DC-link voltage controller is supplemented in the droop control loop, and there is a zero upper limiter at the output of the DC-link voltage controller, which can be enabled or disabled according to the command issued by the microgrid central controller (MGCC) under low-load or high-load operating conditions. Enabling the zero upper limiter means that each of the PV generation systems has excess power reserve and can share the load, while the MPPT only

works when the PV becomes overloaded. Disabling the zero upper limiter can actively start MPPT to ensure full utilization of solar energy under high-load conditions. To find out the dynamic performance of autonomous PV-based MGs under the worst-case scenario, this paper only focuses on high-load operating conditions.

The voltage control loop and current control loop are given in (7) and (8), respectively.

$$\begin{cases} \dot{\phi}_{\mathrm{dPV}i} = \left(i_{\mathrm{ld}}^{\mathrm{PV}i*} - K_{\mathrm{iv}}\phi_{\mathrm{dPV}i} + \omega_n^{\mathrm{PV}i}C_{\mathrm{f}}v_{\mathrm{oq}}^{\mathrm{PV}i} - Hi_{\mathrm{od}}^{\mathrm{PV}i}\right) \\ \qquad /K_{\mathrm{pv}} \\ \dot{\phi}_{\mathrm{qPV}i} = \left(i_{\mathrm{lq}}^{\mathrm{PV}i*} - K_{\mathrm{iv}}\phi_{\mathrm{qPV}i} - \omega_n^{\mathrm{PV}i}C_{\mathrm{f}}v_{\mathrm{od}}^{\mathrm{PV}i} - Hi_{\mathrm{oq}}^{\mathrm{PV}i}\right) \\ \qquad /K_{\mathrm{pv}} \end{cases} \tag{7}$$

$$\begin{cases} \dot{\gamma}_{\mathrm{dPV}i} = \left(v_{\mathrm{id}}^{\mathrm{PV}i*} - K_{\mathrm{ii}}\gamma_{\mathrm{dPV}i} + \omega_n^{\mathrm{PV}i}L_{\mathrm{f}}i_{\mathrm{lq}}^{\mathrm{PV}i}\right)/K_{\mathrm{p}i} \\ \dot{\gamma}_{\mathrm{qPV}i} = \left(v_{\mathrm{iq}}^{\mathrm{PV}i*} - K_{\mathrm{ii}}\gamma_{\mathrm{qPV}i} - \omega_n^{\mathrm{PV}i}L_{\mathrm{f}}i_{\mathrm{ld}}^{\mathrm{PV}i}\right)/K_{\mathrm{p}i} \end{cases} \tag{8}$$

where $\phi_{\mathrm{dPV}i}$ and $\phi_{\mathrm{qPV}i}$ are dynamic states of voltage controller; $i_{\mathrm{ld}}^{\mathrm{PV}i*}$ and $i_{\mathrm{lq}}^{\mathrm{PV}i*}$ are the output signals of the voltage PI regulator; K_{pv} and K_{iv} are gain values of the voltage PI regulator; H and C_{f} are the feedforward gain and filter capacitance, respectively. $\gamma_{\mathrm{dPV}i}$ and $\gamma_{\mathrm{qPV}i}$ are dynamic states of current controller; $v_{\mathrm{id}}^{\mathrm{PV}i*}$ and $v_{\mathrm{iq}}^{\mathrm{PV}i*}$ are the output signals of the current PI regulator; K_{pi} and K_{ii} are gain values of the current PI regulator, and L_{f} is the coupling inductance.

The mathematical model of LCL-filter is given as

$$\begin{cases} \dot{i}_{\mathrm{ld}}^{\mathrm{PV}i} = \left(-R_{\mathrm{f}}i_{\mathrm{ld}}^{\mathrm{PV}i} + \omega_{\mathrm{PV}i}L_{\mathrm{f}}i_{\mathrm{lq}}^{\mathrm{PV}i} + v_{\mathrm{id}}^{\mathrm{PV}i*} - v_{\mathrm{od}}^{\mathrm{PV}i}\right)/L_{\mathrm{f}} \\ \dot{i}_{\mathrm{lq}}^{\mathrm{PV}i} = \left(-R_{\mathrm{f}}i_{\mathrm{lq}}^{\mathrm{PV}i} - \omega_{\mathrm{PV}i}L_{\mathrm{f}}i_{\mathrm{ld}}^{\mathrm{PV}i} + v_{\mathrm{iq}}^{\mathrm{PV}i*} - v_{\mathrm{oq}}^{\mathrm{PV}i}\right)/L_{\mathrm{f}} \\ \dot{v}_{\mathrm{od}}^{\mathrm{PV}i} = \left(\omega_{\mathrm{PV}i}C_{\mathrm{f}}v_{\mathrm{oq}}^{\mathrm{PV}i} + i_{\mathrm{ld}}^{\mathrm{PV}i} - i_{\mathrm{od}}^{\mathrm{PV}i}\right)/C_{\mathrm{f}} \\ \dot{v}_{\mathrm{oq}}^{\mathrm{PV}i} = \left(-\omega_{\mathrm{PV}i}C_{\mathrm{f}}v_{\mathrm{od}}^{\mathrm{PV}i} + i_{\mathrm{lq}}^{\mathrm{PV}i} - i_{\mathrm{oq}}^{\mathrm{PV}i}\right)/C_{\mathrm{f}} \\ \dot{i}_{\mathrm{od}}^{\mathrm{PV}i} = \left(-R_{\mathrm{c}}i_{\mathrm{od}}^{\mathrm{PV}i} + \omega_{\mathrm{PV}i}L_{\mathrm{c}}i_{\mathrm{oq}}^{\mathrm{PV}i} + v_{\mathrm{od}}^{\mathrm{PV}i*} - v_{\mathrm{bd}}^{\mathrm{PV}i}\right)/L_{\mathrm{c}} \\ \dot{i}_{\mathrm{oq}}^{\mathrm{PV}i} = \left(-R_{\mathrm{c}}i_{\mathrm{oq}}^{\mathrm{PV}i} - \omega_{\mathrm{PV}i}L_{\mathrm{c}}i_{\mathrm{od}}^{\mathrm{PV}i} + v_{\mathrm{oq}}^{\mathrm{PV}i*} - v_{\mathrm{bq}}^{\mathrm{PV}i}\right)/L_{\mathrm{c}} \end{cases} \tag{9}$$

where R_{f}, R_{c} and L_{c} are the filter resistance, damping resistance and inductance, respectively; $v_{\mathrm{bd}}^{\mathrm{PV}i}$ and $v_{\mathrm{bq}}^{\mathrm{PV}i}$ represent the bus voltages in local frame.

Since the power calculation loop, droop loop, voltage-current loop and LCL filter models of the BESS are the same as those of the PV system, they will not be repeated here. In addition, to transfer the state variables of each DG to the common frame, DG1 (BESS) is assumed to be the reference frame without loss of generality, and δ_n ($n = 2, 3, \cdots, N$) is defined as the power angle between the nth DG and the common frame, thus

$$\dot{\delta}_n = \omega_n - \omega_{\mathrm{com}} \tag{10}$$

B. Network Model and Load Model

The radiation type network shown in Fig. 1 contains node i ($i = 1, 2, 3$) and line j ($j = 1, 2, 3$), where the relation between the line current $i_{\mathrm{lineD}j}$ and $i_{\mathrm{lineQ}j}$, node voltage $v_{\mathrm{bD}i}$ and $v_{\mathrm{bQ}i}$, as well as the PCC voltage in the common frame v_{bDPCC} and v_{bQPCC}, can be expressed as follows:

$$\begin{cases} \dot{i}_{\mathrm{lineD}j} = (-r_{\mathrm{line}j}i_{\mathrm{lineD}j} + \omega_i L_{\mathrm{line}j}i_{\mathrm{lineQ}j} + v_{\mathrm{bD}i} - v_{\mathrm{bDPCC}}) \\ \qquad /L_{\mathrm{line}j} \\ \dot{i}_{\mathrm{lineQ}j} = (-r_{\mathrm{line}j}i_{\mathrm{lineQ}j} - \omega_i L_{\mathrm{line}j}i_{\mathrm{lineD}j} + v_{\mathrm{bQ}i} - v_{\mathrm{bQPCC}}) \\ \qquad /L_{\mathrm{line}j} \end{cases} \tag{11}$$

where $r_{\mathrm{line}j}$ and $L_{\mathrm{line}j}$ are the feeder impedance of line j; ω_i represents the angle frequency of DGi ($i = 1, 2, 3$). In addition, the mathematical equation of series RL load connected at PCC shown in Fig. 1 are similar to those given in (11).

C. Complete Dynamic Model of the Autonomous PV-based Microgrid

Table I gives the nominal electrical parameters and control parameters related to the MG, which can be used to derive the steady-state operating point data of the model. Linearizing the small-signal model of (1)–(11) around the steady-state operating point and eliminating the intermediate variables provides the small-signal dynamic model of the PV-based MG system.

$$\Delta\dot{\boldsymbol{x}}_{\mathrm{MG}} = \boldsymbol{A}_{\mathrm{MG}}\Delta\boldsymbol{x}_{\mathrm{MG}} \tag{12}$$

$$\Delta\boldsymbol{x}_{\mathrm{MG}} = [\Delta\boldsymbol{x}_{\mathrm{BESS1}} \ \Delta\boldsymbol{x}_{\mathrm{PV1}} \ \Delta\boldsymbol{x}_{\mathrm{PV2}} \ \Delta\boldsymbol{x}_{\mathrm{NET}j} \ \Delta\boldsymbol{x}_{\mathrm{PCCload}}]^{\mathrm{T}} \tag{13}$$

$$\begin{cases} \Delta\boldsymbol{x}_{\mathrm{BESS1}} = [\Delta P_{\mathrm{BESS1}} \ \Delta Q_{\mathrm{BESS1}} \ \Delta\phi_{\mathrm{dqBESS1}} \ \Delta\gamma_{\mathrm{dqBESS1}} \\ \qquad \Delta i_{\mathrm{ldq}}^{\mathrm{BESS1}} \ \Delta v_{\mathrm{odq}}^{\mathrm{BESS1}} \ \Delta i_{\mathrm{odq}}^{\mathrm{BESS1}}]^{\mathrm{T}} \\ \Delta\boldsymbol{x}_{\mathrm{PV1}} = [\Delta V_{\mathrm{DC1}} \ \Delta\delta_2 \ \Delta P_{\mathrm{PV1}} \ \Delta Q_{\mathrm{PV1}} \ \Delta\alpha_{\mathrm{VDC1}} \\ \qquad \Delta\phi_{\mathrm{dqPV1}} \ \Delta\gamma_{\mathrm{dqPV1}} \ \Delta i_{\mathrm{ldq}}^{\mathrm{PV1}} \ \Delta v_{\mathrm{odq}}^{\mathrm{PV1}}\Delta i_{\mathrm{odq}}^{\mathrm{PV1}}]^{\mathrm{T}} \\ \Delta\boldsymbol{x}_{\mathrm{PV2}} = [\Delta V_{\mathrm{DC2}} \ \Delta\delta_3 \ \Delta P_{\mathrm{PV2}} \ \Delta Q_{\mathrm{PV2}} \ \Delta\alpha_{\mathrm{VDC2}} \\ \qquad \Delta\phi_{\mathrm{dqPV2}} \ \Delta\gamma_{\mathrm{dqPV2}} \ \Delta i_{\mathrm{ldq}}^{\mathrm{PV2}} \ \Delta v_{\mathrm{odq}}^{\mathrm{PV2}}\Delta i_{\mathrm{odq}}^{\mathrm{PV2}}]^{\mathrm{T}} \\ \Delta\boldsymbol{x}_{\mathrm{NET}j} = [\Delta i_{\mathrm{lineDQ1}} \ \Delta i_{\mathrm{lineDQ2}} \ \Delta i_{\mathrm{lineDQ3}}]^{\mathrm{T}} \\ \Delta\boldsymbol{x}_{\mathrm{PCCload}} = [\Delta i_{\mathrm{PCCloadDQ}}]^{\mathrm{T}} \end{cases} \tag{14}$$

TABLE I
SYSTEM PARAMETERS OF THE AUTONOMOUS PV-BASED MICROGRID

Parameter	Symbol	Value
	Electrical setup	
Nominal values	$f\left(\omega_n^{\mathrm{PV}i/\mathrm{BESS}i}\right)$, $V_n^{\mathrm{PV}i/\mathrm{BESS}i}$	50 Hz (314 rad/s), 380 V
LCL filter	L_{f}, C_{f}, L_{c}	1.35 mH, 50 μF, 0.35 mH
Feeder impedance	Z_1, Z_2, Z_3	$0.115 + \mathrm{j}0.05$ (Ω)
DC-link voltage capacitor	C_{DC}	1000 μF
	Control parameters	
Rated power	$P_{\mathrm{PV}i/\mathrm{BESS}i}^*$, $Q_{\mathrm{PV}i/\mathrm{BESS}i}^*$	10 kW, 6 kVar
Droop coefficient	$m_{\mathrm{P}}^{\mathrm{PV}i/\mathrm{BESS}i}$, $n_{\mathrm{Q}}^{\mathrm{PV}i/\mathrm{BESS}i}$	$4.7\mathrm{e}^{-5}$, $1.3\mathrm{e}^{-3}$
DC-link voltage controller	K_{pvdc}, K_{ivdc}	$3.15\mathrm{e}^{-4}$, $4.5\mathrm{e}^{-3}$
Voltage controller	K_{pv}, K_{iv}, H	0.05, 390, 0.75
Current controller	K_{pi}, K_{ii}	10.5, $16\mathrm{e}^3$
PV array	$N_{\mathrm{p}i}$, N_{si}, N_{ci}	2, 16, 96
	$I_{\mathrm{rs}i}$, $I_{\mathrm{ph}i}$	$1.1753\mathrm{e}^{-8}$ A, 5.9602 A
	q, k	$1.6022\mathrm{e}^{-19}$ C, $1.3806\mathrm{e}^{-23}$ J/k
	$T_{\mathrm{T}i}$, A_{IF}	298 K, 1.3

where $\Delta x_{\mathrm{BESS1}}$ is the state variable collection of BESS; Δx_{PV1} and Δx_{PV2} are the state variable collections of PV1 and PV2; Δx_{NETj} and $\Delta x_{\mathrm{PCCload}}$ are the state variable collections of the jth line and the PCC load, respectively. Specific elements in the state variable collections represent the corresponding linearized state variable in (1)–(11), e.g., the linearized DC-link voltage variable ΔV_{DC1}, the linearized integral item variable of DC-link voltage controller $\Delta\alpha_{\mathrm{VDC1}}$. The system state matrix $\boldsymbol{A}_{\mathrm{MG}} \in \mathbb{R}^{53\times 53}$ can be obtained from the above ordinary differential equations.

III. Stability Analysis of Autonomous PV-Based MG

A. Participation Factor Analysis

The eigenvalue spectrum of the system state matrix $\boldsymbol{A}_{\mathrm{MG}}$ is usually used for studying the stability and dynamic response of the system [41]. According to classical control theory, the damping ratio ζ of a pair of conjugate eigenvalues $-a \pm jb$ $(a > 0)$ can be calculated as

$$\zeta = a/\sqrt{a^2 + b^2} \tag{15}$$

where a represents the absolute value of the real part and b is the imaginary part of eigenvalues. It should be noted that a smaller a means a slower dynamic response and a lower stability margin, and a lower ζ means the system will behave with worse damping performance, i.e., the system is more prone to oscillation after disturbance. Since the mid-frequency and high-frequency eigenvalues of $\boldsymbol{A}_{\mathrm{MG}}$ are far away from the imaginary axis and their damping ratio is relatively high, the impact of these eigenvalues on the system after encountering disturbances can be ignored. Dominant eigenvalues that mainly determine the dynamics of the system are shown in Fig. 3. In this paper, four pairs of low-frequency eigenvalues, also called low-frequency oscillation modes [42], are numbered as mode m (m = 1, 2, 3, 4) for differentiation according to their real part value at the given steady-state operating point under the parameters of Table I.

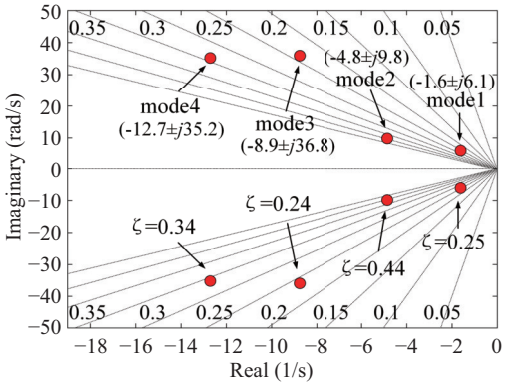

Fig. 3. Low-frequency dominant eigenvalues spectrum of autonomous PV-based MG in the complex plane (where different rays out from the origin represent the constant damping ratios from 0 to 0.35 in steps of 0.05 for eigenvalue locus plots).

Participation factor can further reveal the correlation between the mode and state variables, which can be calculated from left and right eigenvectors of matrix $\boldsymbol{A}_{\mathrm{MG}}$. The participation factor matrix presented in [43] is given by

$$\boldsymbol{PF}_{ij} = \boldsymbol{\Phi}_{ij}\boldsymbol{\Psi}_{ij} \tag{16}$$

where $\boldsymbol{\Phi}_{ij}$ is the right eigenvector and $\boldsymbol{\Psi}_{ij}$ is the left eigenvector. The specific value of the participation factor matrix $\boldsymbol{PF}_{ij}$ reflects observability and controllability from each state variable on every mode. To be more representative, only state variables with normalized participation factors higher than 0.01 are included in Fig. 4. Besides, state variables ΔP, ΔQ, and $\Delta\delta$ which represent power controller dynamic, are collectively defined as the power controller variables here.

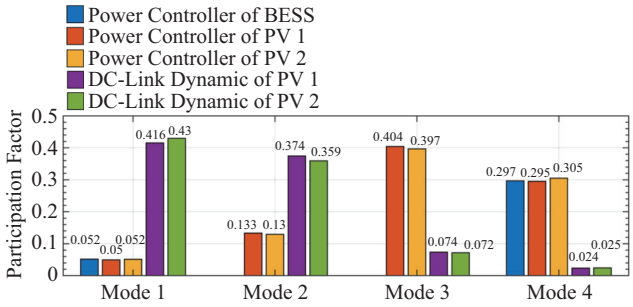

Fig. 4. Participation factor of low-frequency dominant eigenvalues.

In [42], participation factor analysis shows that low-frequency dominant modes are strongly correlated with the power controller variable. However, the conclusion drawn from Fig. 4 is different from that obtained by considering DC-links as ideal voltage sources in [42]. Each dominant mode is related to the DC-link dynamics of PV1 and PV2 to varying degrees, which indicates that dominant modes are determined by the joint effect of power controller variables and DC-link dynamics. According to (2) and (6), power controller variables are mainly determined by the droop coefficient, and DC-link dynamics are determined by the output current of PV panel $i_{\mathrm{PV}i}$ and the inverter-side input currents $i_{\mathrm{DC}i}$ since the capacitor parameter has been set at nominal value. Furthermore, $i_{\mathrm{PV}i}$ is affected by the non-linear V-I characteristic of PV array while $i_{\mathrm{DC}i}$ is related to load change and regulation of DC-link voltage controller (see Section III-C). Therefore, the impact of critical control parameters and non-linear V-I characteristic of PV array on the dynamic characteristics of the autonomous PV-based MG system will be analyzed in the following parts.

B. Impact of Critical Control Parameters

The proportional gain K_{pvdc} and the integral gain K_{ivdc} determine the response speed of the DC-link voltage controller and thus contribute to DC-link dynamics, and the DC-link voltage controller is inserted into the active power droop control loop to jointly determine output angular frequency. To reveal the impact of critical control parameters and the interaction between the DC-link voltage control loop and the active power droop control loop, critical control parameters used for sensitivity analysis are K_{pvdc}, K_{ivdc}, and the active power droop coefficient m_{P}.

Figure 5 shows the traces of autonomous PV-based MG dominant eigenvalues when increasing K_{pvdc} from 0 to

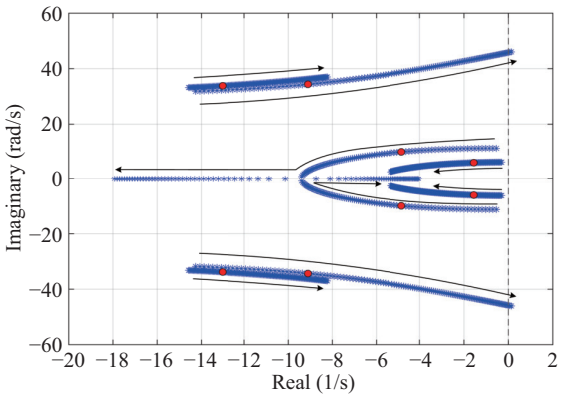

Fig. 5. Traces of autonomous PV-based MG dominant eigenvalues when increasing K_{pvdc} from 0 to 1.26e^{-3} ($m_{\text{P}} = 4.7\text{e}^{-5}$, $K_{\text{ivdc}} = 4.5\text{e}^{-3}$ and red circles are the dominant eigenvalues spectrum in nominal parameters shown in Fig. 3).

1.26e^{-3} and the other parameters are maintained as nominal control parameters. As proportional gain K_{pvdc} is increased, the most dominant modes (mode1 and mode 2) move to the left side and overall stability of the MG system is effectively improved until the negative real part of mode 3 becomes greater than that of mode 1 and mode 2. Enhancement of the damping ratio and stability margin of mode 1 and mode 2 is at the cost of weakening the damping ratio and stability margin of mode 3 and mode 4. Continuous increase in the K_{pvdc} will make mode 3 cross to the right-hand plane and the system becomes unstable.

Figure 6 shows the trajectory of autonomous PV-based MG dominant eigenvalues when K_{ivdc} is increased from 0 to 2e^{-2} and the other parameters are fixed as the nominal parameters. Increasing the integral gain K_{ivdc} will change mode 1 and mode 2 from overdamped to underdamped, i.e., introduce two kinds of oscillation modes into the system. Besides, the damping and stability margin of mode 3 decreases with the increase of K_{ivdc}, and mode 3 will pass through the imaginary axis and enter the right half plane if K_{ivdc} is too large, resulting in system instability.

To study the interaction between the DC-link voltage controller and the active power droop controller, the eigenvalue loci of dominant modes under variation of m_{P} (in the range of 3e^{-5} to 1.19e^{-4}) in different K_{pvdc} and K_{ivdc} (0.6 times, 1 time and 1.4 times of the nominal control parameters, respectively) is presented in Fig. 7. Fig. 7(a), (b) shows that (i) increasing m_{P} always reduces the stability margin of mode 1 and mode 2 even under different K_{pvdc} and K_{ivdc}, and (ii) the simultaneous increase of K_{pvdc} and K_{ivdc} improves the stability margin of mode 1 and mode 2 in various setting of m_{P}. This indicates there is a conflict between the control parameter variation of DC-link voltage controller and the active power droop controller on the system stability margin. Fig. 7(c) shows that (i) an increase of m_{P} degrades the stability margin of mode 3 in the small settings of K_{pvdc} and K_{ivdc} ($\beta = 0.6$), and (ii) enhances the stability margin of mode 3 in the former part while reduces its stability margin in the latter part in relatively large K_{pvdc} and K_{ivdc} ($\beta = 1.0$, $\beta = 1.4$). There is also a conflict for mode 3 in the former part ($\beta = 1.0$, $\beta = 1.4$) since the increased K_{pvdc} and K_{ivdc} make mode 3 move towards the imaginary axis. However, in the latter part, both the increase of m_{P} and β reduce the stability margin of mode 3, and the traces of mode 4 shown in Fig. 7(d) is no exception. In fact, a relatively large m_{P} means that DGs can obtain better power sharing performance, and relatively large K_{pvdc} and K_{ivdc} mean the DC-link voltage controller is more powerful to prevent DC-link voltage from collapsing. Thus, carefully tuned parameters considering the conflict characteristic are conducive to improving both the stability margin of the most dominant oscillation mode and dynamic response speed.

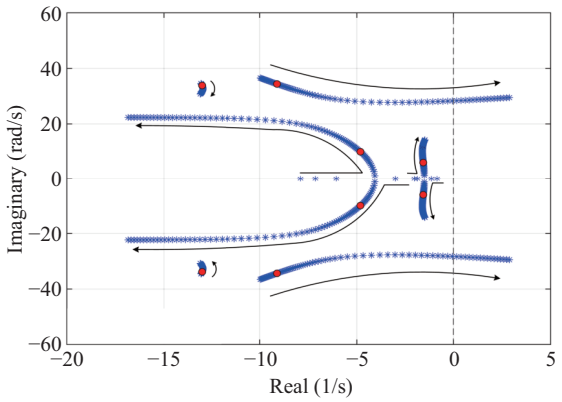

Fig. 6. Traces of autonomous PV-based MG dominant eigenvalues when K_{ivdc} is increased from 0 to 2e^{-2} ($m_{\text{P}} = 4.7\text{e}^{-5}$, $K_{\text{pvdc}} = 3.15\text{e}^{-4}$ and red circles represent the dominant eigenvalues spectrum in nominal parameters shown in Fig. 3).

C. Mechanism of the Oscillation Behavior under Solar Irradiance Change

Since $I_{\text{ph}i}$ is a linear function of the solar irradiation level [21], the non-linear V-I output characteristic of the PV array will also vary according to change of solar irradiance. When solar irradiance is sufficient, $I_{\text{ph}i}$ changes significantly under different solar irradiation level at the MPP, while $V_{\text{DC}i}$ is approximately unchanged at MPP [24]. As a result, if only light intensity increases, it can be seen from (1), (2) (5) and (6) that the increase of $I_{\text{ph}i}$ will enhance the value of $i_{\text{PV}i}$ to $\omega^*_{\text{PV}i}$ in turn. The increase of $\omega^*_{\text{PV}i}$ means the power angle δ_n will be regulated and more active power should be provided by the PV generation system. Then, the additional active power output corresponds to a larger $i_{\text{DC}i}$, which will further reduce the DC-link voltage due to the power unbalance of DC-link. Once the DC-link voltage is lower than the reference voltage $V^{\text{ref}}_{\text{DC}i}$, the DC-link voltage controller will intervene again to prevent the PV system from collapse caused by the continuous drop of the DC-link voltage until it follows $V^{\text{ref}}_{\text{DC}i}$. The entire dynamic interaction process when increasing solar irradiance can be presented in Fig. 8 and vice versa.

As a result of the above analysis, the influence of the non-linear V-I characteristic of the PV array on the dynamic characteristics of MG system can be studied by the relationship between the output angular frequency deviation $\Delta\omega^*_{\text{PV}i}$ and the short-circuit current deviation of the PV panel $\Delta I_{\text{ph}i}$. Since DG1 (BESS) is assumed to be the reference frame, the active power transmission characteristic of the ith PV generation

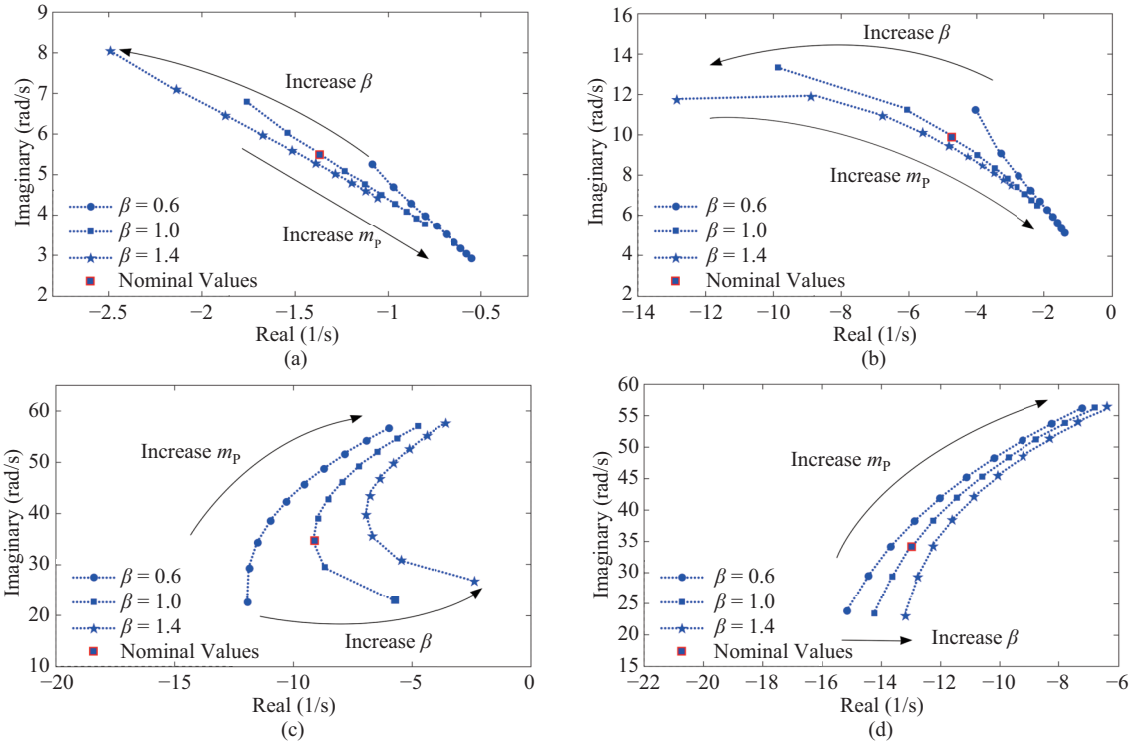

Fig. 7. Traces of dominant modes under variation of m_P from $3e^{-5}$ to $1.19e^{-4}$ in several settings of K_{pvdc} and K_{ivdc} ($K_{pvdc} = \beta \times 3.15e^{-4}$, $K_{ivdc} = \beta \times 4.5e^{-3}$). (a) Mode 1. (b) Mode 2. (c) Mode 3. (d) Mode 4.

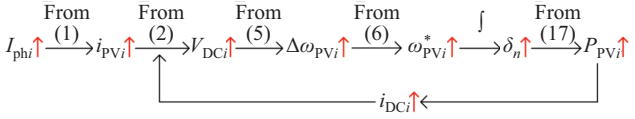

Fig. 8. Dynamic interaction process among relevant variables of PV generation systems when enhancing the solar irradiation level.

system can be expressed as [44]:

$$P_{\mathrm{PV}i} = \left(\frac{E_{\mathrm{PV}i}V_{\mathrm{BESS}}}{Z_i}\cos\delta_n - \frac{V_{\mathrm{BESS}}^2}{Z_i}\right)\cos\theta_i + \frac{E_{\mathrm{PV}i}V_{\mathrm{BESS}}}{Z_i}\sin\delta_n\sin\theta_i \quad (17)$$

where $E_{\mathrm{PV}i}$ is the output voltage amplitude of the ith PV generation; V_{BESS} is the output voltage amplitude of BESS; Z_i and θ_j represent the magnitude and phase of the impedance between the ith PV generation and BESS, respectively.

The transfer function $G_{\mathrm{PV}i}(s)$ between $\Delta\omega^*_{\mathrm{PV}i}$ and $\Delta I_{\mathrm{ph}i}$ can be obtained by combining the small-signal model of (1)–(3), (5), (6) and (17), which is expressed as

$$G_{\mathrm{PV}i}(s) = \frac{\Delta\omega^*_{\mathrm{PV}i}}{\Delta I_{\mathrm{ph}i}} = \frac{K_{\mathrm{pvdc}i}N_{\mathrm{p}i}V^{\mathrm{o}}_{\mathrm{DC}i}s^2 + K_{\mathrm{ivdc}i}N_{\mathrm{p}i}V^{\mathrm{o}}_{\mathrm{DC}i}s}{C_{\mathrm{DC}i}V^{\mathrm{o}}_{\mathrm{DC}i}s^3 + C_{\mathrm{DC}i}V^{\mathrm{o}}_{\mathrm{DC}i}m_{\mathrm{p}}\varepsilon_i s^2 + K_{\mathrm{pvdc}i}\varepsilon_i s + K_{\mathrm{ivdc}i}\varepsilon_i} \quad (18)$$

$$\varepsilon_i = \frac{-E_{\mathrm{PV}i}V_{\mathrm{BESS}}R_i\sin\delta^{\mathrm{o}}_n + E_{\mathrm{PV}i}V_{\mathrm{BESS}}X_i\cos\delta^{\mathrm{o}}_n}{R_i^2 + X_i^2} \quad (19)$$

where R_i and X_i are the resistance and reactance between the ith PV generation and BESS, respectively; the variable with superscript $^{\mathrm{o}}$ is the value of the steady-state operating point.

Oscillation behavior of the studied autonomous PV-based MG system under a sudden change of solar irradiance can be assessed by the difference between $\Delta\omega^*_{\mathrm{PV1}}$ and $\Delta\omega^*_{\mathrm{PV2}}$, that is

$$\Delta\omega^*_{\mathrm{PV2}} - \Delta\omega^*_{\mathrm{PV1}} = \Delta I_{\mathrm{ph2}}G_{\mathrm{PV2}}(s) - \Delta I_{\mathrm{ph1}}G_{\mathrm{PV1}}(s) \quad (20)$$

It can be seen from (18)–(20) that if and only if $\Delta I_{\mathrm{ph1}} = \Delta I_{\mathrm{ph2}}$ and $G_{\mathrm{PV1}}(s) = G_{\mathrm{PV2}}(s)$, $\Delta\omega^*_{\mathrm{PV2}} - \Delta\omega^*_{\mathrm{PV1}} = 0$. Otherwise, $\Delta\omega^*_{\mathrm{PV2}} - \Delta\omega^*_{\mathrm{PV1}} \neq 0$ means the output angular frequency variation of PV1 and PV2 are not in the same step under the sunlight changes. This asynchronous dynamic response will result in frequency oscillation and that will also occur in the active power and DC-link due to the interaction shown in Fig. 8. In fact, owing to partial shading, it is not easy to ensure both $\Delta I_{\mathrm{ph1}} = \Delta I_{\mathrm{ph2}}$ and $G_{\mathrm{PV1}}(s) = G_{\mathrm{PV2}}(s)$, i.e., to ensure $\delta^{\mathrm{o}}_2 = \delta^{\mathrm{o}}_3$ and $V^{\mathrm{o}}_{\mathrm{DC1}} = V^{\mathrm{o}}_{\mathrm{DC2}}$, even if the network parameters, control parameters, and PV array parameters of these two PV generators are identical. Besides, if DC-link voltage is simplified into constant in the modeling process, $\Delta\omega^*_{\mathrm{PV2}} - \Delta\omega^*_{\mathrm{PV1}} \equiv 0$ during sunlight fluctuation, that is, the model will not accurately reflect the oscillation behavior of autonomous PV-based MG during sunlight fluctuation.

Remark 2. Please note the above derivation process is simplified to avoid excessive complexity: (i) the dynamic of inner voltage and current loop is omitted for no contribution to the dominant oscillation modes, (ii) instantaneous active power $p_{\mathrm{PV}i}$ is considered equal to filtered active power $P_{\mathrm{PV}i}$ since damping is mainly governed by the low damping nature of the sinusoidal P–δ dynamics in (17) [12], (iii) $P_{\mathrm{PV}i}$ is assumed

linear with δ_n due to the fact that X_i is sized to make δ_n less than 10° [45].

IV. Distributed Stabilization Controller

Dynamic performance of autonomous PV-based MG will be undesirable during sunlight fluctuation if the initial solar irradiation level and irradiation change of each PV unit are different. Continuous oscillations may threaten stable operation of MG and future urban power energy systems integrated with a large number of PV generations. Therefore, an intelligent distributed stabilization controller based on average consensus algorithm is proposed to suppress the oscillations here.

A. Review of Average Consensus Algorithm

Assuming there are n DGs in the MG, the communication architecture of these DGs can be represented by a weighted graph $G(\nu, \varepsilon, \boldsymbol{A})$, where $\nu = \{1, \cdots, n\}$ is the node set representing n DGs, $\varepsilon \subseteq \nu \times \nu$ is the edge set standing for communication links between any two DGs, and $\boldsymbol{A} = [a_{ij}] \in \mathbb{R}^{n\times n}$ is the weighted adjacency matrix. Further, if $(i, j) \in \varepsilon$ and there is a direct communication link between node i and node j, $a_{ij} = a_{ji} > 0$, and $a_{ij} = a_{ji} = 0$ otherwise.

$$\dot{x}_i = -\sum_{j\in N_i} a_{ij}(x_i - x_j) \tag{21}$$

Equation (21) is an average consensus algorithm, i.e., ensures collective convergence by local interaction, where x_i and x_j are the variables of node i and node j, and represent the frequency f of DGi and DGj here, respectively.

B. Proposed Stabilization Controller

Mathematical expressions of the proposed stabilization controller are:

$$\omega^*_{\mathrm{BESS}i} = \omega_n^{\mathrm{BESS}i} - m_{\mathrm{P}}^{\mathrm{BESS}i}(P_{\mathrm{BESS}i} - P^*_{\mathrm{BESS}i}) + \Delta\omega_{\mathrm{DSC}i} \tag{22}$$

$$\omega^*_{\mathrm{PV}i} = \omega_n^{\mathrm{PV}i} - m_{\mathrm{P}}^{\mathrm{PV}i}(P_{\mathrm{PV}i} - P^*_{\mathrm{PV}i}) + \Delta\omega_{\mathrm{PV}i} + \Delta\omega_{\mathrm{DSC}i} \tag{23}$$

$$\Delta\omega_{\mathrm{DSC}i} = -k\sum_{j\in N_i} a_{ij}(x_i - x_j) \tag{24}$$

where $\Delta\omega_{\mathrm{DSC}i}$ is the supplementary term proposed to stabilize the system; k is the gain that determines the stabilization effect.

The proposed stabilization controller is depicted in Fig. 9. Each DG obtains its neighbor's frequency via the distributed communication layer. Adding a supplementary term to the droop loop makes each DG accelerate to the consensus frequency in transient process and undesirable oscillation caused by the asynchronous dynamic response of each DG will be well avoided. Since the frequencies of all DGs are consistent in steady state, output value of the proposed controller is zero and steady-state performance of the system will not be affected. It should be noted there is no integral term in the proposed controller, which is different from the active power sharing control loop of the distributed secondary controller. Therefore, the proposed controller will not increase the order of the original system and bring unwanted side effects, such as integral saturation phenomenon and oscillatory responses caused by the distributed secondary controller [15].

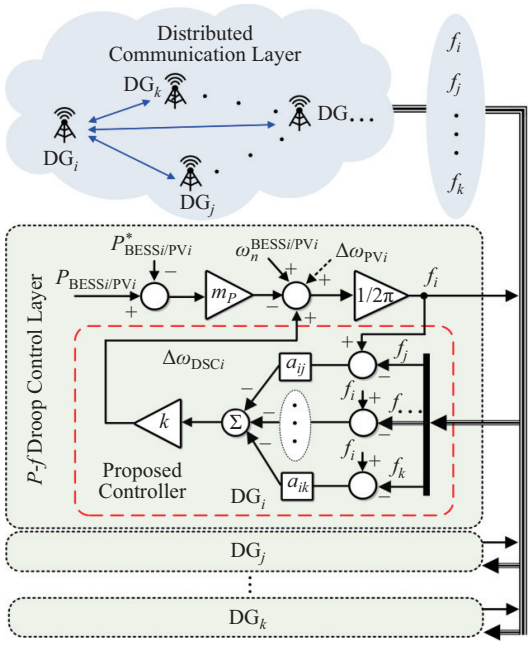

Fig. 9. Diagram of the proposed distributed stabilization controller.

C. Design of Crucial Parameter

The process of parameter tuning can be divided into two steps.

Step 1: Determine the element values in the weighted adjacency matrix $[a_{ij}]$. Element values in the weighted adjacency matrix $[a_{ij}]$ about PV to PV should be designed based on network parameters, control parameters, and PV array parameters to minimize the difference between output angular frequency variation $\Delta\omega^*_{\mathrm{PV}i}$ and $\Delta\omega^*_{\mathrm{PV}j}$. Element values about PV to BESS, and BESS to BESS should be designed according to each rated power since the BESS will bear the responsibility of restraining oscillation if communication links between PV and PV fail, that is, the greater the oscillation energy in the transient process, the greater the energy provided by BESS to suppress the oscillation.

Step 2: Determine parameter k. Parameter k of the proposed controller can be obtained by the trajectory of eigenvalues to improve the specific oscillation mode with relatively low damping ratio.

Suppose that bidirectional communication is provided between each DG in the autonomous PV-based MG. Since network parameters, control parameters, and PV array parameters of PV1 and PV2 are identical, and the rated power of BESS is the same as that of PV in this paper, the element values except for diagonal elements of $[a_{ij}]$ shown in Fig. 10 are considered equal to 1. It should be noted, if the above parameters are different, each element value in the matrix $[a_{ij}]$ should be determined by the eigenvalue traces in turn or the optimization algorithm to obtain an optimal solution.

Considering (22)–(24), the new small-signal dynamic model of MG with the proposed controller can be expressed as

$$\Delta\dot{\boldsymbol{x}}_{\mathrm{MG}} = \boldsymbol{A}^*_{\mathrm{MG}}\Delta\boldsymbol{x}_{\mathrm{MG}} \tag{25}$$

Figure 11 shows the eigenvalue traces of A^*_{MG} when the

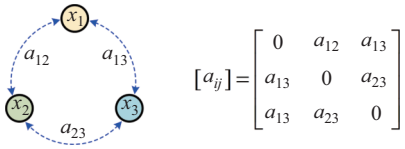

Fig. 10. Distributed communication network of the MG and corresponding weighted adjacency matrix $[a_{ij}]$.

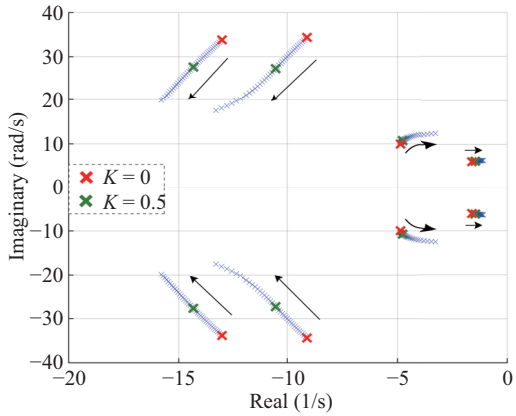

Fig. 11. Traces of dominant eigenvalues as the control parameter k changes from 0 to 1.

value of k changes from 0 to 1. Although there is an inherent trade-off between modes 1, 2 and 3, 4, we propose to increase the damping of mode 3, which is more sensitive to disturbances (see Fig. 14), rather than mode 1 and mode 2. Thus, $k = 0.5$ is an acceptable option for effectively increasing the damping ratio of mode 3 by 50% while exerting a slight impact on mode 1 and mode 2. Note the damping ratio of mode 1 and mode 2 are reduced by only 8% and 6.8%, respectively. Great changes of solar irradiance in a short time will not induce oscillation by mode 1 and mode 2 because the damping ratios of mode 1 and mode 2 are still higher than the recommended value ($\zeta = 0.1$) [46]. Generally, the eigenvalue condition is secure under the disturbance as long as the dominant oscillatory modes are higher than that value.

V. Time-Domain Simulation Results

In order to verify the above analysis, the PV-based MG model is built on the MATLAB/Simulink 2017b platform, where the simulation parameters are from Table I.

A. Dynamic Response without Solar Irradiance Fluctuation

Figure 12 shows the dynamic response of autonomous PV-based MG when $K_{\text{pvdc}} = 0$ and the other parameters are fixed as nominal parameters. Irradiance of PV1 and PV2 is set at a constant value and 3 DGs work in the grid-forming control scheme at the beginning. The DC-link voltage controller is activated at $t = 1$ s. The MG system oscillates for a long time with a frequency of about 1 Hz and 2 Hz before it reaches the steady state, which indicates the decay rate of the dominant oscillation modes is slow and damping is poor. These phenomena meet the eigenvalues spectrum in Fig. 5 that mode 1 (1 Hz) and mode 2 (2 Hz) are close to the imaginary axis when $K_{\text{pvdc}} = 0$.

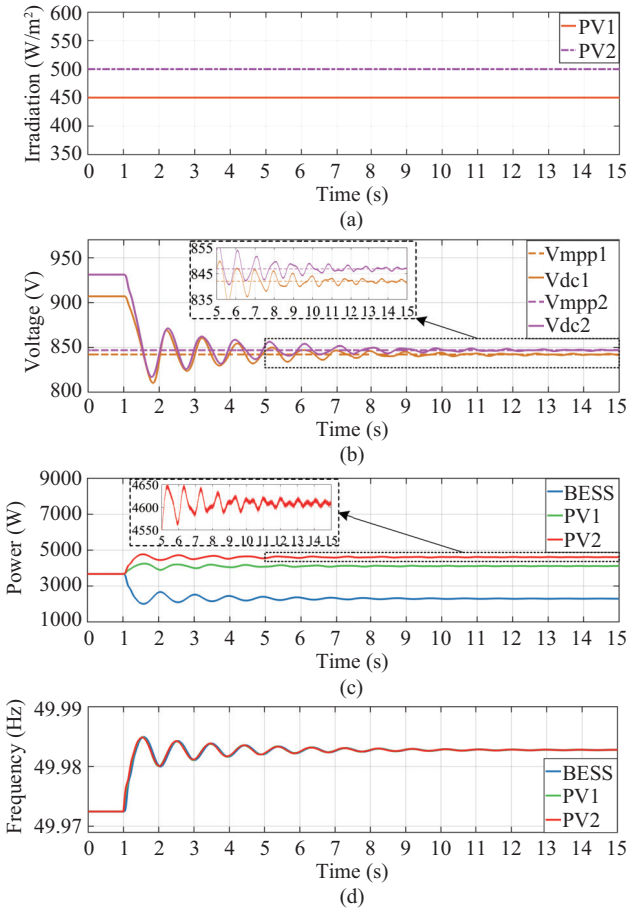

Fig. 12. Dynamic response of autonomous PV-based MG when $K_{\text{pvdc}} = 0$ and the other parameters are fixed as the nominal parameters. (a) Solar irradiation. (b) DC-link voltage. (c) Active power. (d) Frequency.

Figure 13 presents the dynamic response of autonomous PV-based MG under nominal control parameters. The DC-link voltage controller is activated at $t = 1$ s, and a step load of 2 kW increases in PCC bus at $t = 3.5$ s and decreases at $t = 6.5$ s. PV1 and PV2 soon reach their maximum output power after activating the DC-link voltage controller. Moreover, the system dynamic performance is acceptable, and no apparent oscillation is observed under the disturbance of step load. Comparison between Figs. 12 and 13 shows that overall stability of the MG system is effectively improved, which agrees with the sensitive analysis of Section III-B again.

B. Dynamic Response with Solar Irradiance Fluctuation

Figure 14 shows the dynamic response of autonomous PV-based MG under solar irradiance fluctuation, where the initial solar irradiation level and the irradiation change of two PV generators are different. Control parameters are maintained as the nominal values. Note, during this period, the power and frequency of PV1 and PV2 oscillated several times. The oscillation frequency is about 5.9 Hz, which exactly matches the oscillation frequency of mode 3. In addition, .14participation factor results in Fig. 4 show mode 3 is mainly related to the power controller variables of PV1 and PV2, but not to the power controller variables of BESS. Thus, deterioration of mode 3 may cause power oscillation of PV1 and PV2

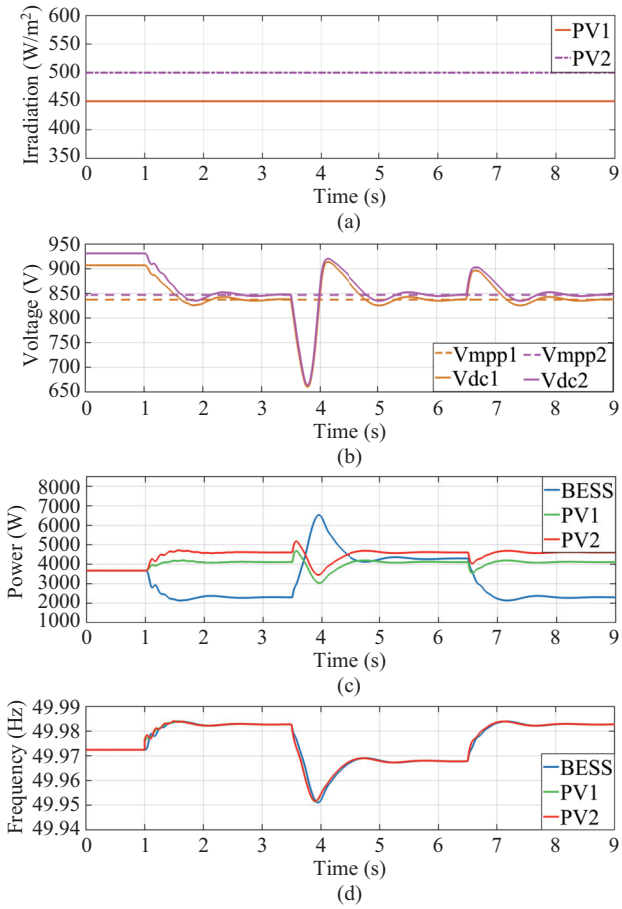

Fig. 13. Dynamic response of autonomous PV-based MG under the nominal parameters. (a) Solar irradiation. (b) DC-link voltage. (c) Active power. (d) Frequency.

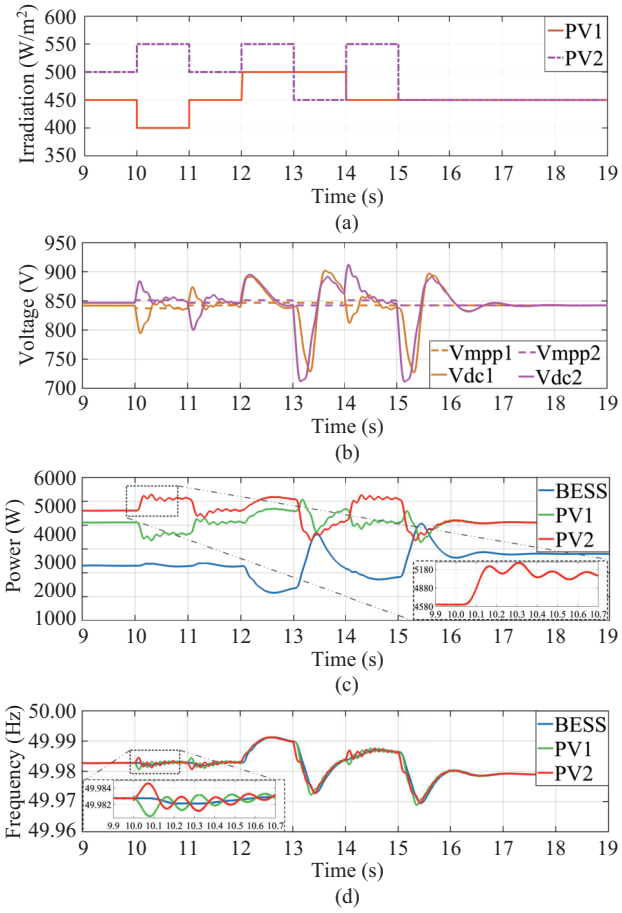

Fig. 14. Dynamic response of autonomous PV-based MG under different initial solar irradiation level and uneven irradiation change. (a) Solar irradiation. (b) DC-link voltage. (c) Active power. (d) Frequency.

under disturbance, while BESS still maintains smooth power injection since it is unobservable from the power controller variables of BESS on mode 3.

Figure 15 presents the dynamic response of autonomous PV-based MG with the same initial solar irradiation level and the same irradiation change. In this case, $\Delta I_{\mathrm{ph1}} = \Delta I_{\mathrm{ph2}}$ and $G_{\mathrm{PV1}}(s) = G_{\mathrm{PV2}}(s)$ is ensured since the steady-state operating point value of δ_n^{o} and $V_{\mathrm{DC}i}^{\mathrm{o}}$ satisfy $\delta_2^{\mathrm{o}} = \delta_3^{\mathrm{o}}$ and $V_{\mathrm{DC1}}^{\mathrm{o}} = V_{\mathrm{DC2}}^{\mathrm{o}}$. As a result, $\Delta\omega_{\mathrm{PV}i}^{*}$ ($\Delta\omega_{\mathrm{PV}i}^{*} \propto \Delta f_{\mathrm{PV}i}$) of PV1 and PV2 is identical and $\Delta\omega_{\mathrm{PV2}}^{*} - \Delta\omega_{\mathrm{PV1}}^{*} = 0$. Obviously, there is no oscillation between PV1 and PV2 under disturbance of solar irradiance fluctuation. Both Figs. 14 and 15 indicate good agreement between the theoretical analysis of Section III-C and time-domain simulation results.

C. Stabilization Effect of the Proposed Controller

The dynamic response of autonomous PV-based MG with the proposed controller when $k = 0.5$ and when $k = 0.2$ are shown in Figs. 16 and 17, respectively. As seen, the oscillation attenuation effect with the proposed controller is better than without the proposed controller by comparing Figs. 16 and 17 with Fig. 14, which verifies the effectiveness of the proposed controller and the selection of k.

Since communication links are essential for the proposed controller, communication link failure is tested to verify the robustness of the proposed controller. Suppose a communication failure occurs between PV1 and PV2 for the proposed distributed controller and a communication failure occurs between traditional centralized controller and PV2. Figs. 18 and 19 present the dynamic response of autonomous PV-based MG under communication link failure with proposed distributed controller and with traditional centralized controller, respectively. Comparison of Figs. 18 and 19 with Fig. 14 indicates traditional centralized controller shows poor oscillation stabilization performance, while the proposed distributed controller shows better robustness in case of communication link failure.

To quantitatively analyze the effect of the proposed controller, we use $\eta = 100\% \times A(t)/A(0)$ to assess the attenuation degree of the oscillation, where $A(0)$ is the initial maximum amplitude of the oscillation and $A(t)$ is the minimum amplitude of the oscillation at a specified period of time. The comparison results about the η of f_{PV2} at three typical period of times under different scenarios are shown in Table II. It can be seen from Table II although the oscillations decay to a certain extent in three different period of times, the dynamic performance is still unsatisfactory since the η of each period of time is still at a relatively large value. After adopting the proposed controller, η can be well reduced to less than 1% at the same time interval when $k = 0.5$ and when

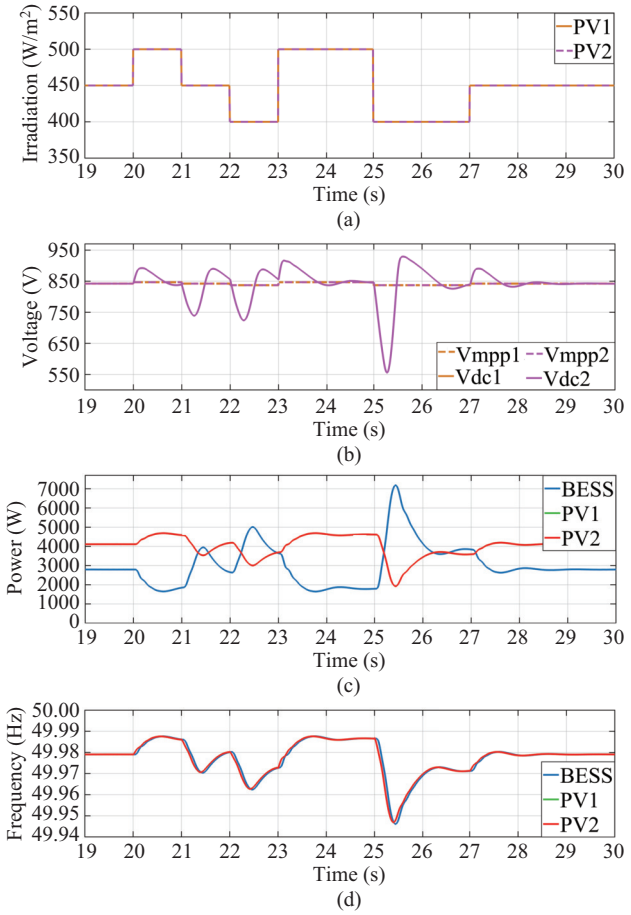

Fig. 15. Dynamic response of autonomous PV-based MG under the same initial solar irradiation level and irradiation change. (a) Solar irradiation. (b) DC-link voltage. (c) Active power. (d) Frequency.

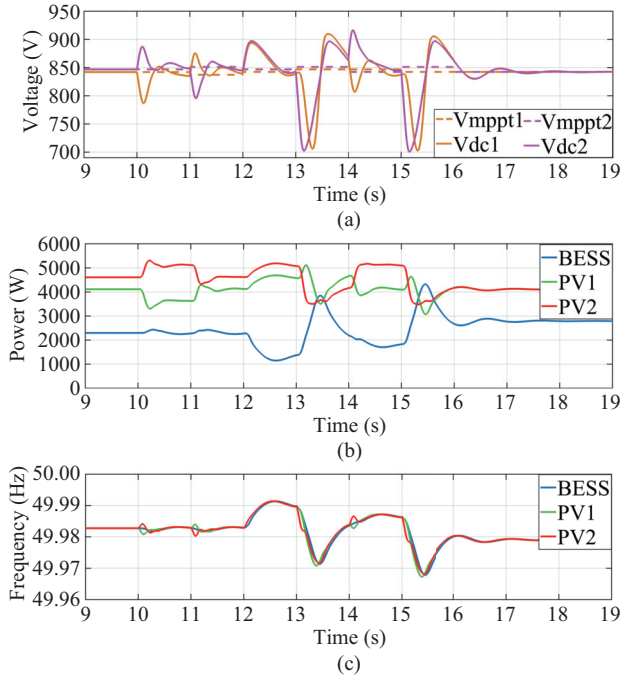

Fig. 16. Dynamic response of autonomous PV-based MG under different initial solar irradiation level and uneven irradiation changes with proposed controller ($k = 0.5$). (a) DC-link voltage. (b) Active power. (c) Frequency.

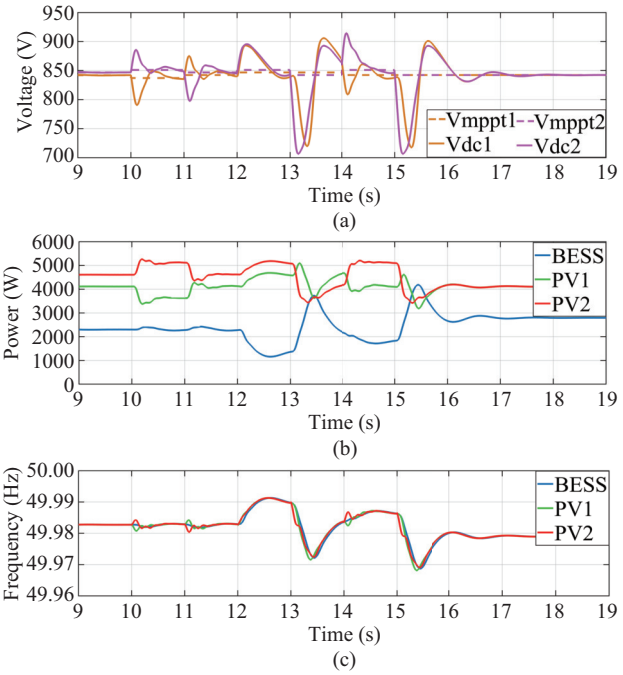

Fig. 17. Dynamic response of autonomous PV-based MG under different initial solar irradiation level and uneven irradiation changes with proposed controller ($k = 0.2$). (a) DC-link voltage. (b) Active power. (c) Frequency.

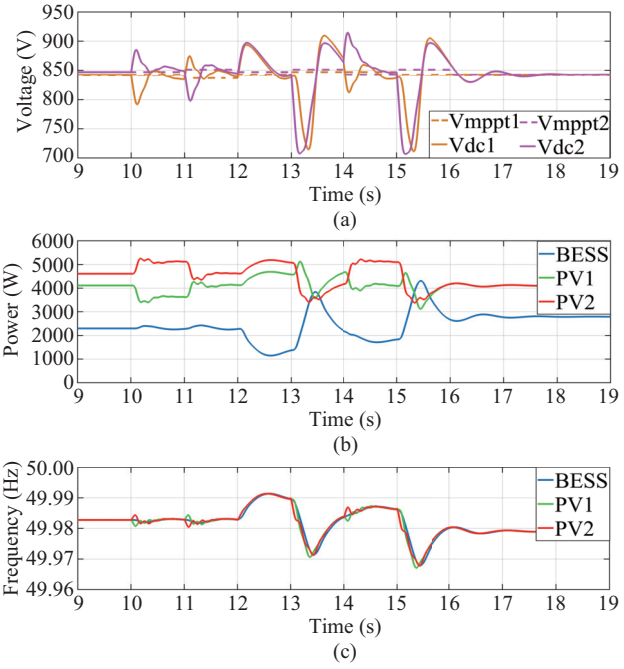

Fig. 18. Dynamic response of autonomous PV-based MG under communication link failure with proposed distributed controller ($k = 0.5$). (a) DC-link voltage. (b) Active power. (c) Frequency.

$k = 0.2$ under normal conditions. Moreover, compared with a traditional centralized controller, the proposed controller possesses more excellent performance on stabling oscillation under communication link failure. Therefore, the proposed stabilization controller can obviously suppress oscillation and is able to provide high reliability and robustness under communication link failure.

TABLE II
COMPARISON RESULTS ABOUT THE η OF f_{PV2} AT THREE TYPICAL PERIODS OF TIME UNDER DIFFERENT SCENARIOS

Time	Without proposed controller ($k = 0$)	With proposed controller ($k = 0.2$)	With proposed controller ($k = 0.5$)	Communication link failure (Proposed distributed controller, $k = 0.5$)	Communication link failure (Traditional centralized controller)
10 s $\leq t <$ 11 s	16.7%	0.9%	0.6%	0.9%	6.7%
11 s $\leq t <$ 12 s	11.5%	0.9%	0.5%	0.8%	6.3%
14 s $\leq t <$ 15 s	12.2%	0.8%	0.5%	0.9%	6.8%

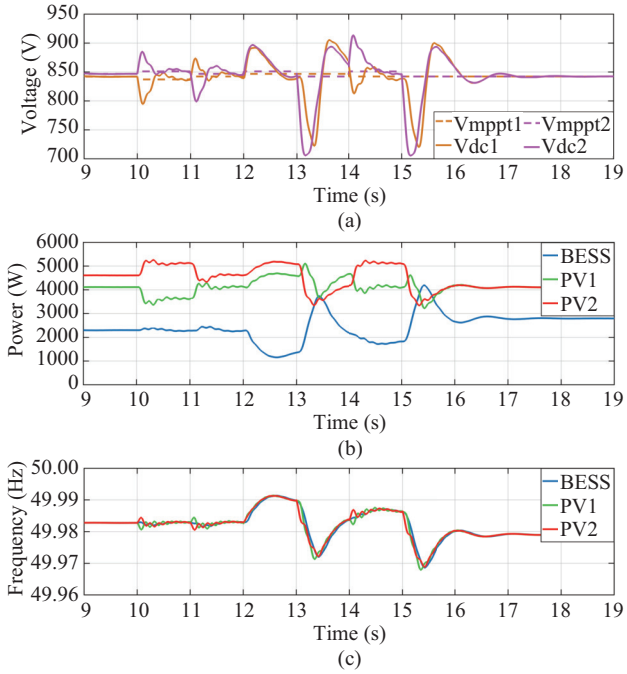

Fig. 19. Dynamic response of autonomous PV-based MG under communication link failure with traditional centralized controller. (a) DC-link voltage. (b) Active power. (c) Frequency.

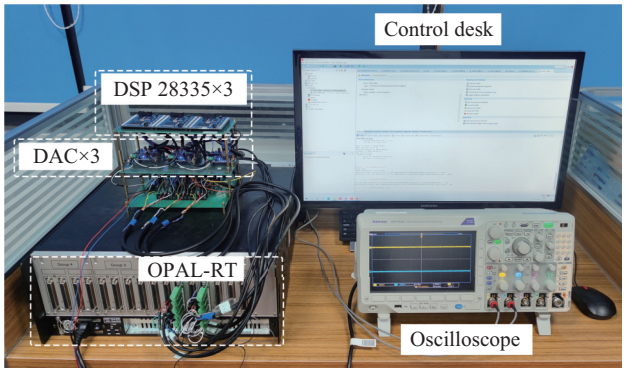

Fig. 20. HIL experimental setup.

VI. HARDWARE-IN-THE-LOOP TEST

In this section, the hardware-in-the-loop (HIL) test is used to verify oscillation caused by DC-link dynamics and the effectiveness of the proposed distributed stabilization controller. Fig. 20 shows the experimental setup. The parameters of the PV-based microgrid in the experimental process are the same with theoretical analysis and simulations in Section III, as given in Table I.

Participation factor analysis in Section III reveals the dynamics of the voltage loop and current loop are independent of the dominant eigenvalues that determine critical dynamic response of the system. Therefore, the proposed stabilization controller, DC-link control loop, droop control loop and power calculation loop are implemented in DSP (TMS320F28335) controller. The main circuit, as well as other control loops are compiled into C code by RT-LAB software installed in control desktop and then downloaded to the OPAL-RT (OP5600) simulator for real-time test.

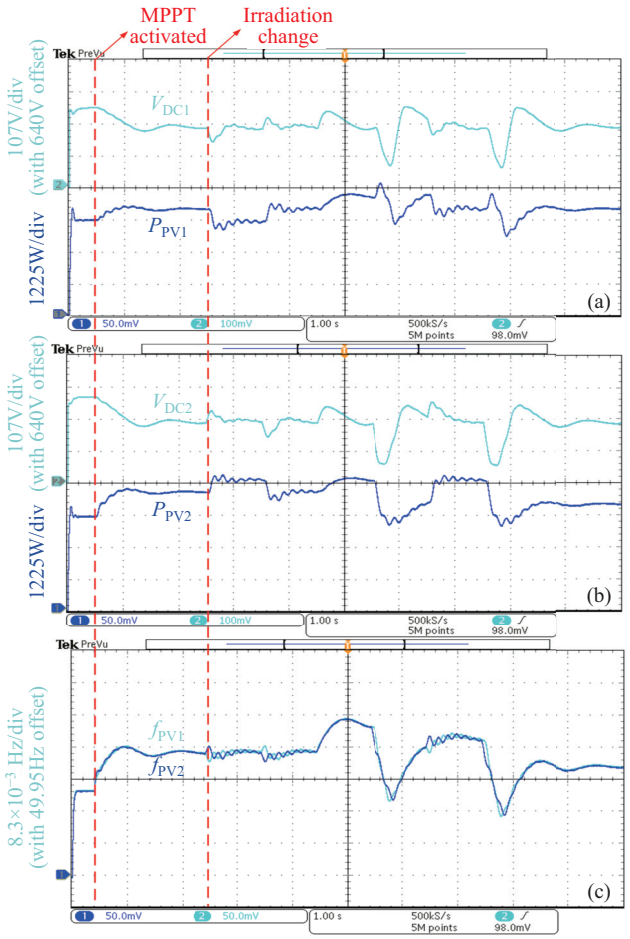

Fig. 21. Dynamic response of autonomous PV-based MG without the proposed controller. (a) DC-link voltage and active power of PV1. (b) DC-link voltage and active power of PV2. (c) Frequency of PV1 and PV2.

The control desktop communicates with the OPAL-RT simulator through LAN and real-time electrical signals are sent out by analog out modules of the OPAL-RT simulator, which can be sampled and by the DSP controller. Then, the calculated reference value of each DG, $\omega^*_{\mathrm{BESS}i/\mathrm{PV}i}$ and $v_{\mathrm{o}}^{\mathrm{BESS}^*/\mathrm{PV}^*}$, are sent to the DAC modules by the serial peripheral interface

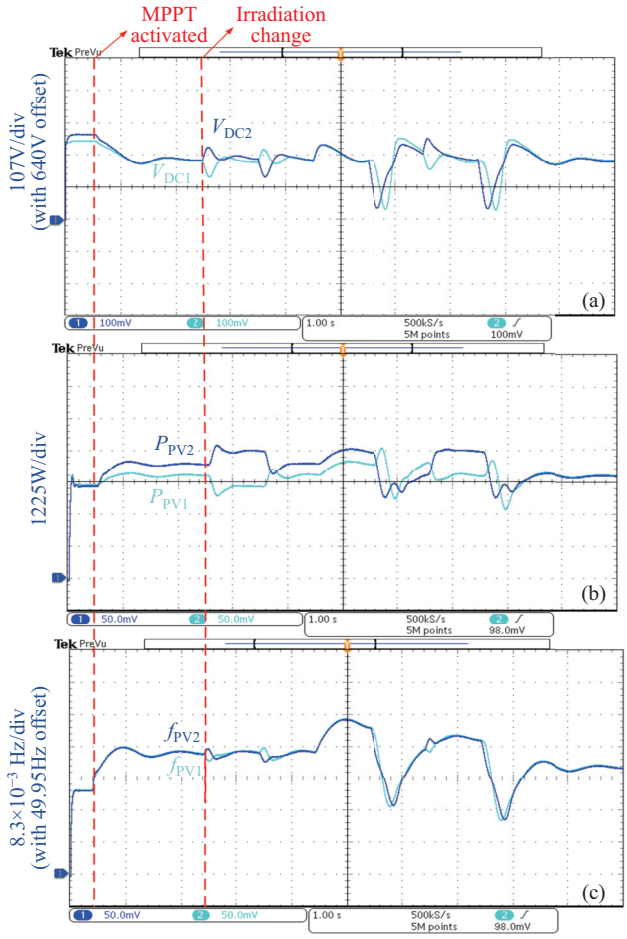

Fig. 22. Dynamic response of autonomous PV-based MG with the proposed controller. (a) DC-link voltage of PV1 and PV2. (b) Active power of PV1 and PV2. (c) Frequency of PV1 and PV2.

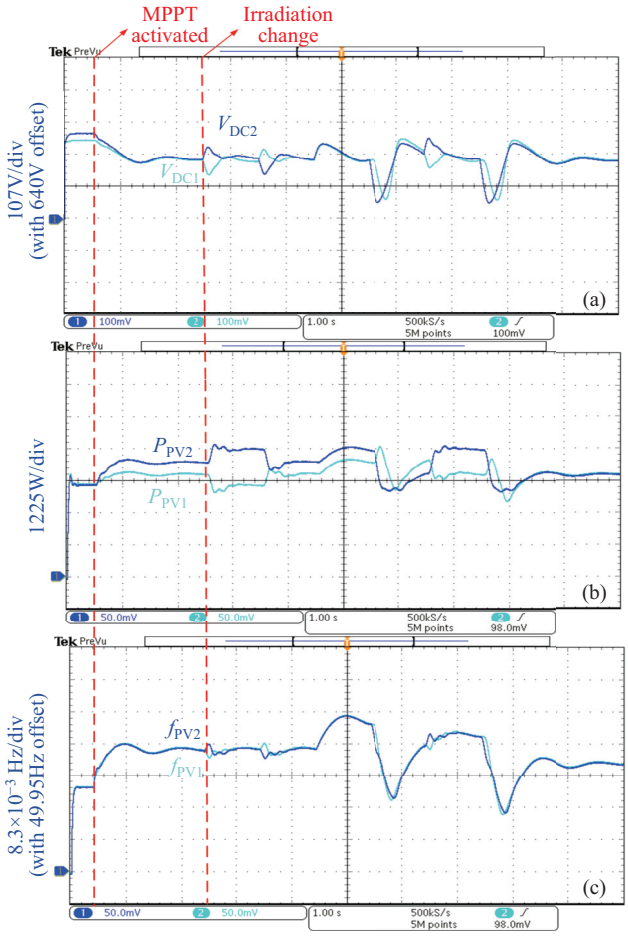

Fig. 23. Dynamic response of autonomous PV-based MG under communication link failure. (a) DC-link voltage of PV1 and PV2. (b) Active power of PV1 and PV2. (c) Frequency of PV1 and PV2.

(SPI). Here, the function of DAC is mainly two-fold: (i) to convert the digital signals $\omega^*_{\mathrm{BESS}i/\mathrm{PV}i}$ and $v_{\mathrm{o}}^{\mathrm{BESS}^*/\mathrm{PV}^*}$ into analog signals and send them back into the OPAL-RT simulator, and (ii) to establish communication links between DG through analog in modules. Communication links are imposed on any two DGs, where the data interconnection is represented by a blue dotted line in Fig. 10. The corresponding DSP controller of each DG can acquire other's frequency signals by sampling the analog output signal $\omega^*_{\mathrm{BESS}i/\mathrm{PV}i}$ of DAC to simulate the communication process. Since the power and frequency of BESS do not oscillate during the transient process, the following analysis will focus on the dynamic response of PV1 and PV2.

A. Dynamic Response without the Proposed Controller

Figure 21 shows the effects of irradiation changes on the DC-link voltage, active power and frequency of the PV systems. It takes 0.5 s from system startup to MPPT activation. After reaching steady state, solar irradiation of PV1 and PV2 starts to change again according to Fig. 14(a) at $t = 2.5$ s. It can be clearly observed that MPPT activation and the moment of significant irradiance change, the DC-link voltage fluctuates significantly, which arouses oscillations of power and frequency corresponding to mode 3 again. At the same time, this specific oscillation also slightly appears in the DC-link voltage due to the dynamic interaction process presented in Fig. 8. Experimental results are consistent with the theoretical analysis once again. Hence, the above results reveal the dynamics of the DC-link cannot be simply ignored in the process of modeling and analysis.

B. Dynamic Response with the Proposed Controller

A comparison between Figs. 21 and 22 shows the effect of the proposed controller. In the transient process, frequency tends to oscillate. However, this poor dynamic response is quickly and effectively improved under the action of the proposed distributed stabilization controller, and smooth power injection is realized. Notably, the introduction of the proposed controller does not change the steady-state performance of the system, nor causes oscillations related to mode 1 and mode 2.

C. Dynamic Response under Communication Link Failure

Suppose a communication failure occurs between PV1 and PV2. Both cannot directly obtain the mutual frequency signal at this time. Comparing Figs. 23 and 21 presents even in case of communication failure, the remaining communication network can still enable PV to obtain more desirable dynamic

performance. Therefore, the robustness of the proposed controller is verified again in the HIL test.

VII. Conclusion

This paper reveals the undesirable oscillations that occur during specific irradiance changes in autonomous PV-based MG and provides a solution to the oscillation problem caused by DC-link dynamics. A detailed dynamic model of autonomous PV-based MG is built for analysis. Stability analysis results show that: (i) DC-link dynamics also contribute to dominant eigenvalues, unlike previous conclusions obtained by ignoring DC-link dynamics and (ii) essential influence factors of the DC-link dynamics include critical control parameters and non-linear V-I characteristics of PV array. As a result, oscillation will occur between different PV generators if critical control parameters are not adjusted properly or under disturbance of uneven sunlight changes with different initial DC-link voltage. Based on the average consensus algorithm, a distributed stabilization controller is proposed to overcome undesirable oscillation. Finally, hardware-in-the-loop test proves the proposed controller can effectively suppress oscillation without affecting the steady-state performance of the system under normal and communication link failure conditions.

References

[1] L. M. Jia, J. Ma, P. Cheng, and Y. K. Liu, "A perspective on solar energy-powered road and rail transportation in China," *CSEE Journal of Power and Energy Systems*, vol. 6, no. 4, pp. 760–771, Dec. 2020.

[2] S. F. Abdelsamad, W. G. Morsi, and T. S. Sidhu, "Probabilistic impact of transportation electrification on the loss-of-life of distribution transformers in the presence of rooftop solar photovoltaic," *IEEE Transactions on Sustainable Energy*, vol. 6, no. 4, pp. 1565–1573, Oct. 2015.

[3] M. Sechilariu, B. C. Wang, and F. Locment, "Building integrated photovoltaic system with energy storage and smart grid communication," *IEEE Transactions on Industrial Electronics*, vol. 60, no. 4, pp. 1607–1618, Apr. 2013.

[4] M. J. E. Alam, K. M. Muttaqi, and D. Sutanto, "A three-phase power flow approach for integrated 3-wire MV and 4-wire multigrounded LV networks with rooftop solar PV," *IEEE Transactions on Power Systems*, vol. 28, no. 2, pp. 1728–1737, May 2013.

[5] X. J. Quan, R. Y. Yu, X. Zhao, Y. Lei, T. X. Chen, C. J. Li, and A. Q. Huang, "Photovoltaic synchronous generator: architecture and control strategy for a grid-forming PV energy system," *IEEE Journal of Emerging and Selected Topics in Power Electronics*, vol. 8, no. 2, pp. 936–948, Jun. 2020.

[6] M. Malinowski, J. I. Leon, and H. Abu-Rub, "Solar photovoltaic and thermal energy systems: current technology and future trends," *Proceedings of the IEEE*, vol. 105, no. 11, pp. 2132–2146, Nov. 2017.

[7] L. J. Chen and S. W. Mei, "An integrated control and protection system for photovoltaic microgrids," *CSEE Journal of Power and Energy Systems*, vol. 1, no. 1, pp. 36–42, Mar. 2015.

[8] A. S. A. Awad, M. F. Shaaban, T. H. M. El-Fouly, E. F. El-Saadany, and M. M. A. Salama, "Optimal resource allocation and charging prices for benefit maximization in smart PEV-parking lots," *IEEE Transactions on Sustainable Energy*, vol. 8, no. 3, pp. 906–915, Jul. 2017.

[9] Y. M. Zhang and L. Cai, "Dynamic charging scheduling for EV parking lots with photovoltaic power system," *IEEE Access*, vol. 6, pp. 56995–57005, Oct. 2018.

[10] W. Jiang and Y. Q. Zhen, "A real-time EV charging scheduling for parking lots with pv system and energy store system," *IEEE Access*, vol. 7, pp. 86184–86193, Jun. 2019.

[11] J. M. Guerrero, J. C. Vasquez, J. Matas, L. G. de Vicuna, and M. Castilla, "Hierarchical control of droop-controlled AC and DC microgrids—a general approach toward standardization," *IEEE Transactions on Industrial Electronics*, vol. 58, no. 1, pp. 158–172, Jan. 2011.

[12] Y. A. R. I. Mohamed and E. F. El-Saadany, "Adaptive decentralized droop controller to preserve power sharing stability of paralleled inverters in distributed generation microgrids," *IEEE Transactions on Power Electronics*, vol. 23, no. 6, pp. 2806–2816, Nov. 2008.

[13] X. F. Wang, F. Blaabjerg, and Z. Chen, "Autonomous control of inverter-interfaced distributed generation units for harmonic current filtering and resonance damping in an islanded microgrid," *IEEE Transactions on Industry Applications*, vol. 50, no. 1, pp. 452–461, Jan./Feb. 2014.

[14] X. Q. Guo, Z. G. Lu, B. C. Wang, X. F. Sun, L. Wang, and J. M. Guerrero, "Dynamic phasors-based modeling and stability analysis of droop-controlled inverters for microgrid applications," *IEEE Transactions on Smart Grid*, vol. 5, no. 6, pp. 2980–2987, Nov. 2014.

[15] X. Y. Wu and C. Shen, "Distributed optimal control for stability enhancement of microgrids with multiple distributed generators," *IEEE Transactions on Power Systems*, vol. 32, no. 5, pp. 4045–4059, Sep. 2017.

[16] X. Zhang, H. Zhang, M. Li, Z. X. Guo, Y. H. Hu, Q. D. Chen, X. X. Liu, and F. Li, "Analysis of dynamic power angle oscillation and its suppression strategy for the droop-controlled grid-connected inverter," *IEEE Journal of Emerging and Selected Topics in Power Electronics*, vol. 9, no. 5, pp. 5718–5731, Oct. 2021.

[17] M. Ahmed, F. Alsokhiry, A. S. Abdel-Khalik, K. H. Ahmed, and Y. Al-Turki, "Improved damping control method for grid-forming converters using LQR and optimally weighted feedback control loops," *IEEE Access*, vol. 9, pp. 87484–87500, Jun. 2021.

[18] A. Saim, A. Houari, J. M. Guerrero, A. Djerioui, M. Machmoum, and M. A. Ahmed, "Stability analysis and robust damping of multiresonances in distributed-generation-based islanded microgrids," *IEEE Transactions on Industrial Electronics*, vol. 66, no. 11, pp. 8958–8970, Nov. 2019.

[19] R. Majumder, B. Chaudhuri, A. Ghosh, R. Majumder, G. Ledwich, and F. Zare, "Improvement of stability and load sharing in an autonomous microgrid using supplementary droop control loop," *IEEE Transactions on Power Systems*, vol. 25, no. 2, pp. 796–808, May 2010.

[20] J. Selvaraj and N. A. Rahim, "Multilevel inverter for grid-connected PV system employing digital PI controller," *IEEE Transactions on Industrial Electronics*, vol. 56, no. 1, pp. 149–158, Jan. 2009.

[21] A. Yazdani and P. P. Dash, "A control methodology and characterization of dynamics for a photovoltaic (PV) system interfaced with a distribution network," *IEEE Transactions on Power Delivery*, vol. 24, no. 3, pp. 1538–1551, Jul. 2009.

[22] R. A. Mastromauro, M. Liserre, and A. Dell'Aquila, "Control issues in single-stage photovoltaic systems: MPPT, current and voltage control," *IEEE Transactions on Industrial Informatics*, vol. 8, no. 2, pp. 241–254, May 2012.

[23] C. Y. Tang, Y. T. Chen, and Y. M. Chen, "PV power system with multi-mode operation and low-voltage ride-through capability," *IEEE Transactions on Industrial Electronics*, vol. 62, no. 12, pp. 7524–7533, Dec. 2015.

[24] R. Gules, J. D. P. Pacheco, H. L. Hey, and J. Imhoff, "A maximum power point tracking system with parallel connection for PV stand-alone applications," *IEEE Transactions on Industrial Electronics*, vol. 55, no. 7, pp. 2674–2683, Jul. 2008.

[25] T. V. Thang, A. Ahmed, C. I. Kim, and J. H. Park, "Flexible system architecture of stand-alone PV power generation with energy storage device," *IEEE Transactions on Energy Conversion*, vol. 30, no. 4, pp. 1386–1396, Dec. 2015.

[26] S. Sen and V. Kumar, "Simplified modeling and HIL validation of solar PVs and storage-based islanded microgrid with generation uncertainties," *IEEE Systems Journal*, vol. 14, no. 2, pp. 2653–2664, Jun. 2020.

[27] W. Du, Q. R. Jiang, M. J. Erickson, and R. H. Lasseter, "Voltage-source control of PV inverter in a CERTS microgrid," *IEEE Transactions on Power Delivery*, vol. 29, no. 4, pp. 1726–1734, Aug. 2014.

[28] Y. H. Xia, M. Yu, X. M. Wang, and W. Wei, "Describing function method based power oscillation analysis of *LCL*-filtered single-stage PV generators connected to weak grid," *IEEE Transactions on Power Electronics*, vol. 34, no. 9, pp. 8724–8738, Sep. 2019.

[29] S. M. Malik, Y. Y. Sun, X. Ai, Z. Q. Chen, and K. Y. Wang, "Small-signal analysis of a hybrid microgrid with high PV penetration," *IEEE Access*, vol. 7, pp. 119631–119643, Aug. 2019.

[30] T. Zhao, X. Zhang, W. Mao, F. S. Wang, J. Xu, and Y. L. Gu, "A modified hybrid modulation strategy for suppressing DC voltage fluctuation of cascaded H-bridge photovoltaic inverter," *IEEE Transactions on Industrial Electronics*, vol. 65, no. 5, pp. 3932–3941, May 2018.

[31] Y. H. Hu, X. Zhang, W. Mao, T. Zhao, F. S. Wang, and Z. Q. Dai, "An optimized third harmonic injection method for reducing DC-link voltage fluctuation and alleviating power imbalance of three-phase cascaded H-bridge photovoltaic inverter," *IEEE Transactions on Industrial Electronics*, vol. 67, no. 4, pp. 2488–2498, Apr. 2020.
[32] Y. H. Shan, J. F. Hu, and J. M. Guerrero, "A model predictive power control method for PV and energy storage systems with voltage support capability," *IEEE Transactions on Smart Grid*, vol. 11, no. 2, pp. 1018–1029, Mar. 2020.
[33] Z. Moradi-Shahrbabak and A. Tabesh, "Effects of front-end converter and DC-link of a utility-scale PV energy system on dynamic stability of a power system," *IEEE Transactions on Industrial Electronics*, vol. 65, no. 1, pp. 403–411, Jan. 2018.
[34] H. D. Cai, J. Xiang, and W. Wei, "Modelling, analysis and control design of a two-stage photovoltaic generation system," *IET Renewable Power Generation*, vol. 10, no. 8, pp. 1195–1203, Sep. 2016.
[35] R. H. Lasseter, J. H. Eto, B. Schenkman, J. Stevens, H. Vollkommer, D. Klapp, E. Linton, H. Hurtado, and J. Roy, "CERTS microgrid laboratory test bed," *IEEE Transactions on Power Delivery*, vol. 26, no. 1, pp. 325–332, Jan. 2011.
[36] Z. L. Zhao, P. Yang, Y. W. Wang, Z. R. Xu, and J. M. Guerrero, "Dynamic characteristics analysis and stabilization of PV-based multiple microgrid clusters," *IEEE Transactions on Smart Grid*, vol. 10, no. 1, pp. 805–818, Jan. 2019.
[37] Y. L. Xu, W. Zhang, M. Y. Chow, H. B. Sun, H. B. Gooi, and J. C. Peng, "A distributed model-free controller for enhancing power system transient frequency stability," *IEEE Transactions on Industrial Informatics*, vol. 15, no. 3, pp. 1361–1371, Mar. 2019.
[38] Y. Song, D. J. Hill, T. Liu, and Y. Zheng, "A distributed framework for stability evaluation and enhancement of inverter-based microgrids," *IEEE Transactions on Smart Grid*, vol. 8, no. 6, pp. 3020–3034, Nov. 2017.
[39] Z. Y. Tang, D. J. Hill, T. Liu, and Y. Song, "Distributed inter-area oscillation damping control for power systems by using wind generators and load aggregators," *International Journal of Electrical Power & Energy Systems*, vol. 123, pp. 106201, Dec. 2020.
[40] M. X. Shi, X. Chen, J. Y. Zhou, Y. Chen, J. Y. Wen, and H. B. He, "Frequency restoration and oscillation damping of distributed VSGs in microgrid with low bandwidth communication," *IEEE Transactions on Smart Grid*, vol. 12, no. 2, pp. 1011–1021, Mar. 2021.
[41] Y. N. Chi, B. J. Tang, J. B. Hu, X. S. Tian, H. Y. Tang, Y. Li, S. J. Sun, L. Shi, and L. Shuai, "Overview of mechanism and mitigation measures on multi-frequency oscillation caused by large-scale integration of wind power," *CSEE Journal of Power and Energy Systems*, vol. 5, no. 4, pp. 433–443, Dec. 2019.
[42] N. Pogaku, M. Prodanovic, and T. C. Green, "Modeling, analysis and testing of autonomous operation of an inverter-based microgrid," *IEEE Transactions on Power Electronics*, vol. 22, no. 2, pp. 613–625, Mar. 2007.
[43] P. Kundur, *Power System Stability and Control*, New York, NY, USA: McGraw-Hill, 1994.
[44] A. R. Bergen, *Power Systems Analysis*, Englewood Cliffs, NJ: Prentice Hall, 1986.
[45] R. H. Lasseter, "MicroGrids," in *Proceedings of 2002 IEEE Power Engineering Society Winter Meeting*, New York, USA, 2002, pp. 305–308.
[46] B. Pal and B. Chaudhuri, *Robust Control in Power Systems*, New York, NY, USA: Springer, 2005.

Zhuoli Zhao (S'15–M'18) received a Ph.D. degree in Electrical Engineering from South China University of Technology, Guangzhou, China, in 2017. From October 2014 to December 2015, he was a Joint Ph.D. Student and Sponsored Researcher with the Control and Power Research Group, Department of Electrical and Electronic Engineering, Imperial College London, London, U.K. He is currently an Associate Professor with the School of Automation, Guangdong University of Technology, Guangzhou, China. His research interests include microgrid control and energy management, modeling, analysis and control of power-electronized power systems and smart grids.

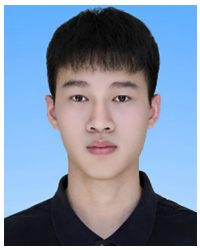

Jindian Xie received a B.E. degree from Dongguan University of Technology, Dongguan, China, in 2020. He is currently working toward the master's degree in Electrical Engineering with the School of Automation, Guangdong University of Technology, Guangzhou, China. His research interests include stability analysis and control of microgrid.

Shaoqing Gong received a B.E. degree in Electrical Engineering from Changchun University of Science and Technology, Changchun, China, in 2020. He is currently studying for a master's degree from Guangdong University of Technology, Guangzhou, China. His research interests include model predictive control of smart grids.

Xi Luo received a B.E. degree from Guangdong University of Technology, Guangzhou, China, in 2020. He is currently working toward a master's degree in Electrical Engineering with the School of Automation, Guangdong University of Technology, Guangzhou, China. His research interests include control of renewable power generation and microgrid.

Yuewu Wang received his Ph.D. degree in Electrical Engineering from South China University of Technology, Guangzhou, China, in 2017. In 2020, he joined the Guangxi University of Science and Technology, Liuzhou, China, where he is currently a Lecturer. His current research interests include pulse width modulation techniques, DC-DC converters and grid-connected inverters.

Chun Sing Lai (S'11–M'19–SM'20) received a D.Phil. degree in Engineering Science from the University of Oxford, Oxford, UK, in 2019. He is currently a Lecturer with the Department of Electronic and Electrical Engineering, Brunel University London. His current research interests are in power system optimization and data analytics.

Ping Yang (M'11) received a Ph.D. degree in Automatic Control from South China University of Technology, Guangzhou, China, in 1998. She is currently a Professor with the School of Electric Power Engineering, South China University of Technology, Guangzhou, China and the Director of Guangdong Key Laboratory of Clean Energy Technology, South China University of Technology, Guangzhou, China. Her current research interests include smart microgrid and electricity market.

Loi Lei Lai (M'87–SM'92–F'07–LF'21) received a B.S. (First Class Hons.), Ph.D., and D.S. degrees in Electrical and Electronic Engineering from the University of Aston, Birmingham, UK, and City, University of London, London, UK, in 1980, 1984, and 2005, respectively. He is currently a University Distinguished Professor with Guangdong University of Technology, Guangzhou, China. His current research areas are in smart cities and smart grid.

Josep M. Guerrero (S'01–M'04–SM'08–F'15) received a B.Sc. degree in Telecommunications Engineering, a M.Sc. degree in Electronics Engineering, and a Ph.D. degree in Power Electronics from the Technical University of Catalonia, Barcelona, in 1997, 2000 and 2003, respectively. Since 2011, he has been a Full Professor with AAU Energy, Aalborg University, Denmark. His research interests are oriented to different microgrid frameworks in applications.